Spectroscopic Observations of the Solar Corona during the 2017 August 21 Total Solar Eclipse: Comparison of Spectral Line Widths and Doppler Shifts Between Open and Closed Magnetic Structures

Yingjie Zhu (朱英杰) [ID],[1, *] Shadia R. Habbal [ID],[2] Adalbert Ding [ID],[3, 4] Bryan Yamashiro,[2] Enrico Landi [ID],[1] Benjamin Boe [ID],[5, 2] Sage Constantinou [ID],[2] and Michael Nassir [ID][2]

[1] Department of Climate and Space Sciences and Engineering, University of Michigan,
Ann Arbor, MI 48109, USA
[2] Institute for Astronomy, University of Hawaii, 2680 Woodlawn Drive, Honolulu, HI, USA
[3] Institute of Optics and Atomic Physics, Technische Universität Berlin, Berlin, Germany
[4] Institut für Technische Physik, Berlin, Germany
[5] Wentworth Institute of Technology, Boston, MA 02115, USA

ABSTRACT

The spectroscopic observations presented here were acquired during the 2017 August 21 total solar eclipse with a three-channel partially multiplexed imaging spectrometer (3PAMIS) operating at extremely high orders (> 50). The $4\,R_\odot$ extent of the slit in the North-South direction scanned the corona starting from the central meridian out to approximately $1.0\,R_\odot$ off the east limb throughout totality. The line widths and Doppler shifts of the Fe X (637.4 nm) and Fe XIV (530.3 nm) emission lines, characteristic of 1.1×10^6 K and 1.8×10^6 K electron temperatures respectively, varied across the different coronal structures intercepted by the slit. Fe XIV was the dominant emission in the closed fields of an active region and the base of a streamer, with relatively constant 20 - 30 km s^{-1} line widths independent of the height. In contrast, Fe X emission exhibited broader (> 40 km s^{-1}) line widths in open fields which increased with height, in particular in the polar coronal hole. Inferences of line widths and Doppler shifts were consistent with extreme ultraviolet (EUV) observations from Hinode/EIS, as well as with the near-infrared Fe XIII 1074 nm line observed by CoMP. The differences in the spectral line widths between distinct coronal structures are interpreted as an indication of the predominance of wave heating in open structures versus localized heating in closed structures. This study underscores the unparalleled advantages and the enormous potential of TSE spectroscopy in measuring line widths simultaneously in open and closed fields at high altitudes, with minimal exposure times, stray light levels, and instrumental widths.

1. INTRODUCTION

Corresponding author: Yingjie Zhu (朱英杰)
yingjie.zhu@pmodwrc.ch

* DKIST Ambassador.
Now at Physikalisch Meteorologisches Observatorium Davos, World Radiation Center (PMOD/WRC), 7260 Davos, Switzerland

Total solar eclipse (TSE) spectroscopic observations of the 'green' line in 1869 by Young and Harkness led to the discovery of a 1.8×10^6 K coronal electron temperature, when its correct identification as Fe XIV emission at 530.3 nm was made by Grotrian (1939) and Edlén (1943). Following this seminal discovery, TSE spectroscopic observations have been pursued in earnest. They led to the discovery of a rich coronal spectrum with different ionization states of elements, such as Ni, Ar, and

Ca, to name a few (see Jefferies et al. 1971). In addition to inferences of the electron temperature (e.g., Boe et al. 2022, 2023), and chemical composition, spectral lines offer fundamental diagnostic tools such as inferences of the ion effective temperature (Del Zanna & DeLuca 2018), which include contributions from ion temperatures and nonthermal motions along the line of sight. Doppler shifts, when present, yield mass motions, both steady and dynamic.

The list of identified emission lines in the early TSE spectroscopic observations did not always report the same emission lines. Furthermore, decades of spectroscopic observations also differed in the observed line widths and their variations across the corona,(Kim 2000; Koutchmy et al. 2005; Raju et al. 2011; Prabhakar et al. 2019). These differences can be readily accounted for by differences in the underlying structures, covering a range of electron temperatures, as resolved by complementary imaging observations of coronal emission lines during totality (e.g., Habbal et al. 2011, 2021; Boe et al. 2018).

Despite their paucity, TSE spectral and imaging data remain unique scientific assets for exploring the properties of the different manifestations of coronal heating and solar wind acceleration mechanisms responsible for these observables. The uniqueness of these observations stems from the properties of the emission from coronal forbidden lines, which is dominated by radiative excitation (Habbal et al. 2007). This property enables the detection of the emission out to much larger distances than extreme ultraviolet imaging and spectroscopy, as the latter lines are dominated by collisional excitation, hence detectable only at shorter distances.

This paper presents an analysis of spectroscopic observations of the Fe X 637.4 nm and Fe XIV 530.3 nm lines obtained during the 2017 August 21 TSE. They capitalize on the distinct advantage of the spatial extent of emission from coronal forbidden lines spanning at least $1\,R_\odot$ above the limb, thus exploring a range of different coronal structures. The primary focus of the analysis is on the spectral line widths from which the effective ion temperature can be inferred, and on any Doppler shifts when present. The spectral observations are placed in the context of emission line imaging of Fe XI 789.2 nm and Fe XIV 530.3 nm acquired at the same time (Boe et al. 2020). The eclipse observations are complemented by spectroscopic observations of extreme ultraviolet (EUV) lines taken with the EUV Imaging Spectrograph (EIS; Culhane et al. 2007) on board the Hinode spacecraft (Kosugi et al. 2007) as well as in the Fe XIII 1074.7 nm near-infrared line with the ground-based Coronal Multichannel Polarimeter (CoMP; Tom-

czyk et al. 2008). The observations, including methodology and the specifics of the spectrometer, are given in Section 2. The ancillary space-based and ground-based observations are presented in Section 3. This is followed by a discussion including comparisons between the different instruments in Section 4. Concluding remarks with a summary of the outstanding findings and their implications are given in Section 5.

2. 3PAMIS OBSERVATIONS AND RESULTS

2.1. *Operation and Data Acquisition*

During the 2017 TSE, spectroscopic observations were obtained using a three-channel PArtially Multiplexed Imaging Spectrometer (3PAMIS). The 3PAMIS has a design similar to the dual-channel (2PAMIS) spectrometer used at the 2015 TSE (Ding & Habbal 2017).

With this spectrometer, the eclipsed Sun is imaged onto a slit mirror using a tele lens (NIKON ED Nikkor $f = 300\,\mathrm{mm}$, F/2.8). The transmitted light is made parallel by a collimator lens (ASKANIA Askinar $f = 100\,\mathrm{mm}$, F/1.9), and then passed through three dichroic mirrors which separate the spectrum into three wavelength bands: blue(400–500 nm), green(500–610 nm), and red(610–1100 nm). The light from each of these regions is dispersed by three diffraction gratings into different output angles, depending on the wavelength and the diffraction order. Each of the three beams is focused onto a CCD camera (ATIK Infinity) with a lens system (NIKON Nikkor $f = 50\,\mathrm{mm}$, F/1.8). Schott color filters (cut-off and bandpass filters) are used to correct the limitations of the dichroic mirrors.

A monitor camera captures the solar image reflected by the slit mirror and determines the slit position with respect to the Sun. Our analysis of the detector images showed that the chromium slit mirror coating is slightly transparent, resulting in ghost images of the solar limb and of bright prominences which are superimposed onto the coronal spectrum.

The emission of Fe XIV (530.3 nm) is observed in the green channel, and that of Fe X (637.4 nm) is in the red channel along with other spectral lines (H, He, Fe XI,...), all in very high orders. The Fe XIV emission is captured from 60th to 64th orders, while the Fe X 637.4 nm line is recorded from 51st to 53rd orders. In addition to the spectral lines, the electron K-corona and F-corona continuum were also observed (Boe et al. 2021). However, the stacking of multiple orders of the white light continuum on the detector made its interpretation challenging. The wavelength scale of the green detector is approximately $0.025\,\mathrm{nm\,px^{-1}}$, and the red detector has a wavelength scale of around $0.030\,\mathrm{nm\,px^{-1}}$, yielding a resolution power $R \sim 20{,}000$.
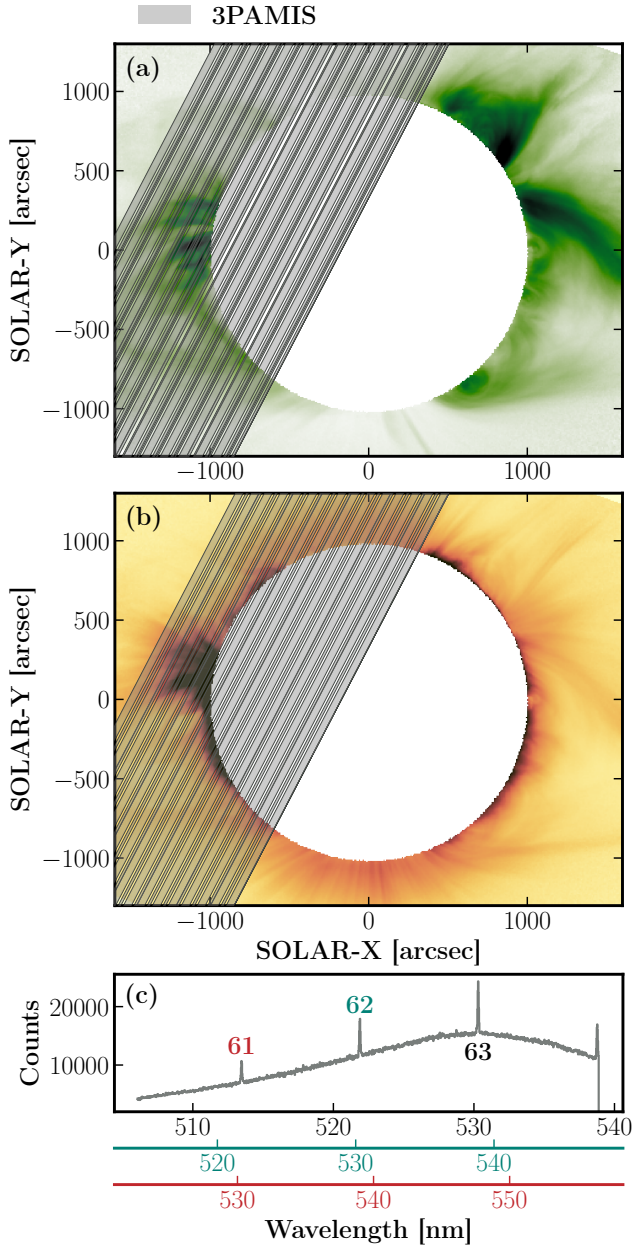
Figure 1. Overview of the 3PAMIS observation during the 2017 TSE and two Hinode/EIS observations made on 2017 August 21. (a) 3PAMIS/Green FOV (gray) overplotted on the Fe XIV 530.3 nm line-to-continuum ratio image. The darker gray lines indicate the start and end times of each exposure. (b) 3PAMIS/Red FOV (gray) overplotted on the Fe XI 789.2 nm line-to-continuum ratio image. (c) An example streamer spectrum showing Fe XIV 530.3 nm line at the 61st, 62nd, and 63rd orders. Link to the `Jupyter` notebook creating this figure: ⊙.

The 3PAMIS spectra covered a region corresponding to 4 $R_\odot$ along the slit direction. The pixel size is equivalent to 8″3 in the spatial dimension. The spatial reso-

lution perpendicular to the slit depends on the exposure time of each raster. This is because 3PAMIS made a sit-and-stare observation, with the Sun gradually moving across the slit as time went by.

During the eclipse, the 3PAMIS data presented here were acquired at Guernsey State Park, Wyoming, USA, at 42°18′585, W 104°47′206, and an altitude of 1406 m. Totality began at 17:45:37 UT (second contact), when the Sun was 55°.4 above the horizon, and ended at 17:47:56 UT (third contact). At the start of the totality, the slit was initially placed along the central meridian, tilted slightly from the solar northwest to southeast. The tracking motion of the mount was then disabled, and the Sun slowly drifted across the slit, enabling the acquisition of the coronal spectrum above the east limb. 3PAMIS made intermittent exposures when the slit scanned the east limb, leaving data gaps between each exposure due to the finite readout and download time of the two CCD detectors (see Figure 1a and b). The typical exposure times of the green detector were repeating sequentially at 0.5 s, 1 s, and 3 s, while for the red detector, they were 1 s and 3 s.

The 3PAMIS data were corrected and calibrated through dark frame subtraction, curvature correction, and flat-fielding. In addition, the wavelength calibration was performed and the instrumental broadening was measured from the calibration frames taken in the laboratory. The 3PAMIS pointing was determined using the slit position in the context images and was coaligned with the narrow-bandpass images. The details of data reduction and calibration procedures are presented in Appendix A.

Figure 1c shows an example spectrum from the green detector, including the Fe XIV 530.3 nm line at 61st, 62nd, and 63rd orders and the stacked multi-order continuum. The ambient continuum was first removed by a linear fit and followed by a single-Gaussian fit to the strongest orders of Fe XIV 530.3 nm (63rd) and Fe X 637.4 nm (52nd) line. Line profiles in different orders were not co-added because the camera was best focused on the strongest orders, and the wavelength scale varies with orders (see more discussion in Appendix C). To maximize the S/N in fitting Doppler velocities and line widths, data were averaged over 5 pixels along the slit.

2.2. *Data Analysis and Results*

Figure 2 shows the line-to-continuum maps and line profiles of Fe XIV 530.3 nm and Fe X 637.4 nm observed in the off-limb regions. The profiles are obtained by averaging five pixels along the slit and removing the multi-order continuum. The intensity maps reveal several structures at the east limb, including the NOAA
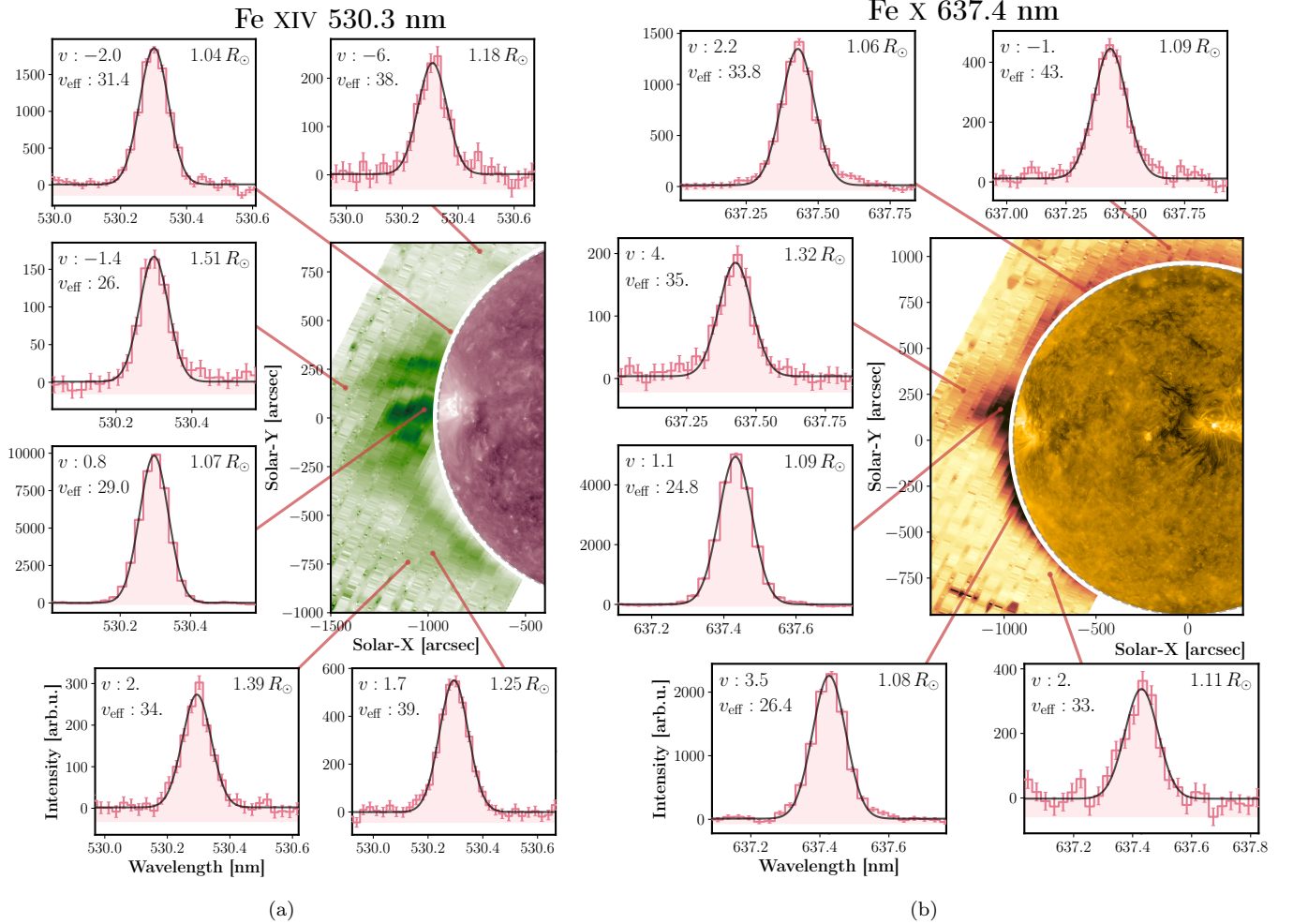
Figure 2. Overview of the Fe XIV 530.3 nm (left) and Fe X 637.4 nm (right) line intensities observed by 3PAMIS. The line-to-continuum ratios of the two lines are shown, along with the SDO/AIA images on the disk. To fill the data gaps, the intensity is interpolated using a 2-D Gaussian convolution kernel. The small zoom-in panels show Fe XIV 530.3 nm and Fe X 637.4 nm line profiles, which are binned over 5 pixels along the slit. Additionally, single-Gaussian fit results of these profiles are shown. v represents the Doppler velocity, and $v_{\rm eff}$ denotes the effective velocity, both of which are in units of $\rm km\,s^{-1}$. Link to the `Jupyter` notebook creating this figure: ⟳.

active region (AR) 12672 near the equator, a streamer in the northeast direction, and another streamer in the southeast (also see Boe et al. 2020). Global magnetohydrodynamic (MHD) simulations and white light observations confirmed that a streamer cusp and polar plumes from a low-latitude coronal hole (CH) at the far side contributed to the emission in the northeast region (Mikić et al. 2018). With 1-3 s exposures and spatial binning of approximately 40″ along the slit, the Fe XIV 530.3 nm profiles can be fitted up to 1.5 $R_{\odot}$ in the AR, while the Fe X 637.4 nm line can be observed up to 1.3 $R_{\odot}$.

The Fe XIV emission appears most prominent above the AR, while other diffuse emission is observed in the southern streamer. Notably, the Fe XIV 530.3 nm profiles in the AR are narrower than the fainter Fe XIV profiles

in streamers. Most Fe X emission forms close to the limb, below 1.1 $R_{\odot}$, except for the northern boundary of the AR. The Fe X profiles in the northern CHs are remarkably broader than the Fe X profiles in the close-field regions.

The fitting results of Fe X and Fe XIV are shown in Figure 3. Panel d displays the relative line-to-continuum ratio of Fe XIV, demonstrating similarities to the line-to-continuum ratio measured using narrow-bandpass filters shown in Figure 3a, using the technique described by Boe et al. (2020).

Figure 3e shows the Doppler shifts in Fe XIV 530.3 nm line. The Doppler velocities in the AR vary within $\pm 2\,\rm km\,s^{-1}$. Larger Doppler shifts are evident in the southern and northern streamers. The northern
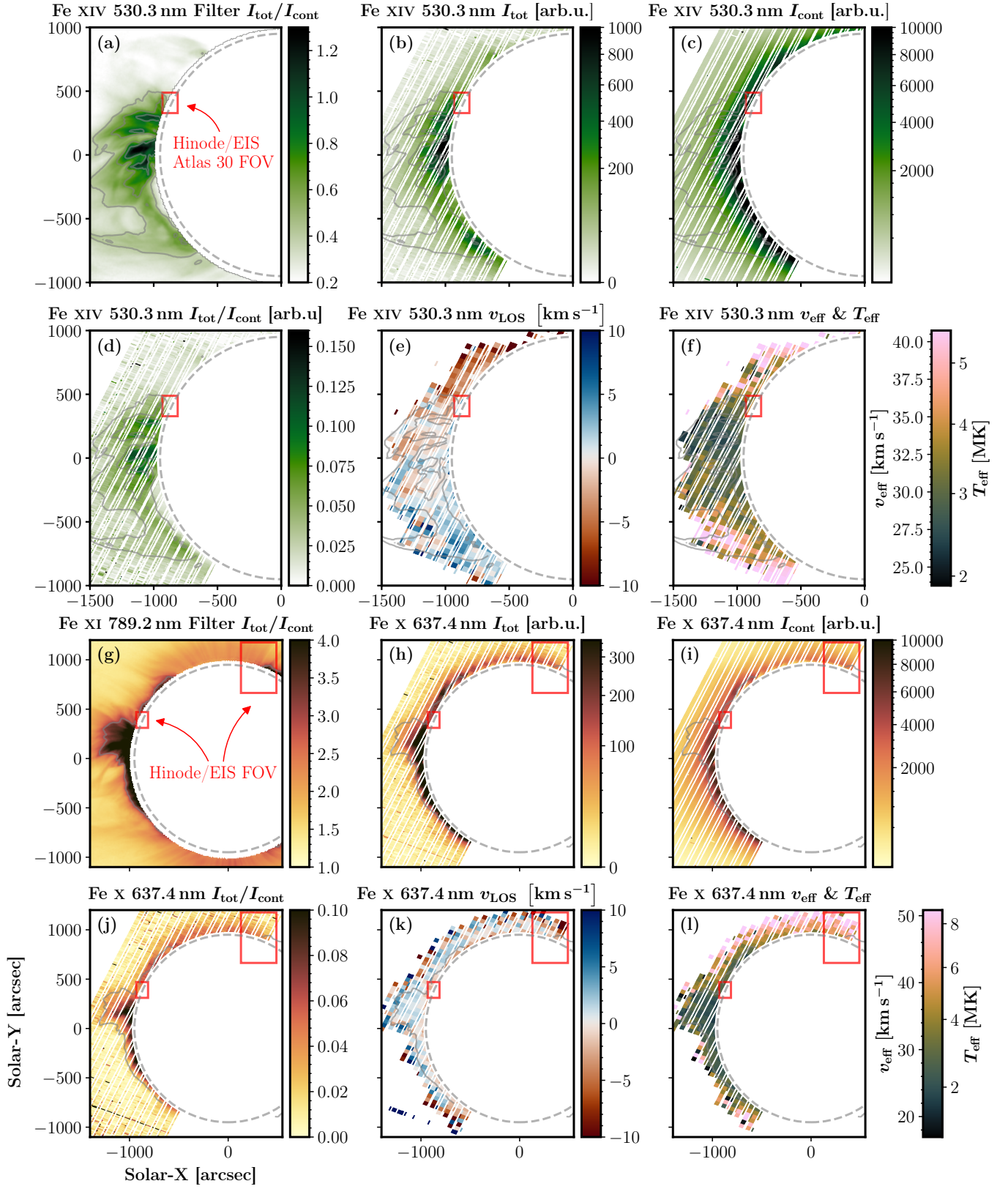
Figure 3. (a) Fe XIV 530.3 nm line-to-continuum ratio measured by a narrow-bandpass imager from Boe et al. (2020). (b) 3PAMIS Fe XIV 530.3 nm line intensity. (c) ambient continuum intensity. (d) line-to-continuum ratio. (e) Doppler velocity. (f) line width. (g) Fe XI 789.2 nm narrow-band image. (h-l) similar to panels (b-f) but for Fe X 637.4 nm. The red rectangles represent the FOVs of two complementary Hinode/EIS observations. The gray contours outline the intensity structures in Fe XIV (panels a to f) and Fe X (panels g to l) narrow bandpass images. Link to the Jupyter notebook creating this figure: Ω.

streamer exhibits a redshift of up to $5\text{–}10\,\mathrm{km\,s^{-1}}$, while the southern streamer reveals a blueshift of approximately $5\,\mathrm{km\,s^{-1}}$.

It is often assumed that the observed full width at half maximum (FWMH) $\Delta\lambda_{\mathrm{true}}$ consists of a thermal width associated with the ion temperature T_i and a non-thermal width ξ caused by other unresolved motions (Del Zanna & Mason 2018):

$$\Delta\lambda_{\mathrm{true}} = \left[4\ln 2\left(\frac{\lambda_0}{c}\right)^2\left(\frac{2k_B T_i}{m_i} + \xi^2\right)\right]^{1/2} \quad (1)$$

where λ_0 is the wavelength of the spectral line, c is the speed of light, k_B is the Boltzmann constant, and m_i represents the ion mass. To represent the width of different spectral lines with various λ_0, we introduced the effective velocity v_{eff} or effective temperature T_{eff} as

$$v_{\mathrm{eff}}^2 = \frac{2k_B T_{\mathrm{eff}}}{m_i} \equiv \frac{2k_B T_i}{m_i} + \xi^2 \quad (2)$$

Notably, v_{eff} is equivalent to the $1/e$ velocity $v_{1/e}$ used in other publications (e.g., Wilhelm et al. 2005). As depicted in Figure 3f, the typical Fe XIV line widths in the off-limb AR range from 25 to $32\,\mathrm{km\,s^{-1}}$. These line widths correspond to effective temperatures of 2.1–3.5 MK. In comparison, the Fe XIV line profiles in the northern and southern streamers are much broader. The effective velocities in these streamers are in the range of $v_{\mathrm{eff}} = 35\text{–}40\,\mathrm{km\,s^{-1}}$, equivalent to $T_{\mathrm{eff}} = 4.2\text{–}5.4\,\mathrm{MK}$.

Panels h to l of Figure 3 display the fitting results of the Fe X 637.4 nm line. Due to the lack of calibrated Fe X 637.4 nm narrow bandpass images, the line intensity to continuum ratio of the Fe XI 789.2 nm line, which has a similar formation temperature, is shown in panel a for comparison. Most Fe X line emission forms near the limb. The enhancement of Fe X emission in the AR appears to be located between the two other loop-like structures observed in Fe XIV, indicating the existence of cold ($\sim$1 MK) loops or plasma outflows in the vicinity of the hot (2 MK) AR (also see Boe et al. 2020).

The Doppler shifts of Fe X 637.4 nm, shown in Figure 3k, range between -5 and $5\,\mathrm{km\,s^{-1}}$, which is within the uncertainty of the absolute wavelength calibration of 3PAMIS. In the AR and quiet Sun (QS) corona, Fe X shows an effective velocity v_{eff} of $20\text{–}25\,\mathrm{km\,s^{-1}}$, corresponding to an effective temperature T_{eff} of approximately 2 MK. On the other hand, the Fe X line in the CH, is similar to other observations (e.g., Hahn et al. 2012), as it shows extreme broadening with $v_{\mathrm{eff}} > 40\,\mathrm{km\,s^{-1}}$. The effective temperature T_{eff} of Fe X in the CH exceeds 6 MK, suggesting the presence of significant nonthermal velocities or additional heating of the Fe X ion.

Panels a–c of Figure 4 depict the variation of Fe XIV 530.3 nm line intensity and widths along four different cuts in various structures. Compared to Fe XIV in the AR, the Fe XIV lines in streamers are dimmer by at least a factor of 2. Fe XIV line intensities show a nearly exponential decrease in all four regions below a heliocentric distance of approximately $1.4\,R_\odot$. Above this distance, the Fe XIV intensity decreases more slowly with height. This behavior might be attributed to the increase in photoexcitation to populate the upper energy level, the limitation of the instrument sensitivity, or the radial dependence in the hydrostatic and isothermal atmosphere (Aschwanden 2005) as

$$p(r) = p_0 \exp\left[-\frac{r - R_\odot}{\lambda_p(T_e)} \cdot \frac{R_\odot}{r}\right] \quad (3)$$

where p_0 is the pressure at the surface, r denotes the heliocentric distance, and $\lambda_p(T_e)$ is the hydrostatic scale height. The intensity drop was fitted with the hydrostatic model along the cut in the southern streamer, noting that $I(r) \propto p(r)^2$ when collisional excitation dominates (also see Discussion in Section 4.1.1). We found a hydrostatic scale height λ_p of approximately 100 Mm in the streamer, corresponding to a temperature of around 2 MK.

Regarding the Fe XIV line widths, they appear to be nearly constant along the two cuts in the AR, showing an effective temperature T_{eff} of approximately 2.5 - 3 MK.

The variation of Fe X 637.4 nm line intensity and width along four different cuts is shown in Panels d–f of Figure 4. The Fe X line intensity decreases exponentially with height up to $1.3\,R_\odot$ along these cuts. Similar to Fe XIV, the Fe X line width in the AR slightly increases from 20 to $25\,\mathrm{km\,s^{-1}}$ between $1.0\text{–}1.3\,R_\odot$. The Fe X widths in the QS below $1.15\,R_\odot$ also remains relatively constant at $v_{\mathrm{eff}} \approx 25\,\mathrm{km\,s^{-1}}$. In contrast, the Fe X line widths in the CH show a drastic increase from 40 to $60\,\mathrm{km\,s^{-1}}$ between 1.1 and $1.2\,R_\odot$, reaching an effective temperature greater than 10 MK above $1.2\,R_\odot$. Notably, the Fe X line widths in the northeast region appear to be slightly broader than those in the AR below $1.1\,R_\odot$, but narrower than Fe XIV in the same region. However, its width increases from 25 to $50\,\mathrm{km\,s^{-1}}$ between $1.1\text{–}1.2\,R_\odot$, approaching the Fe X widths in the CH observed by 3PAMIS . This behavior might be attributed to the transition of the emission from the streamer cusp to polar plumes as height increases.

3. COMPARISON WITH ANCILLARY SPACE-BASED AND GROUND-BASED DATA
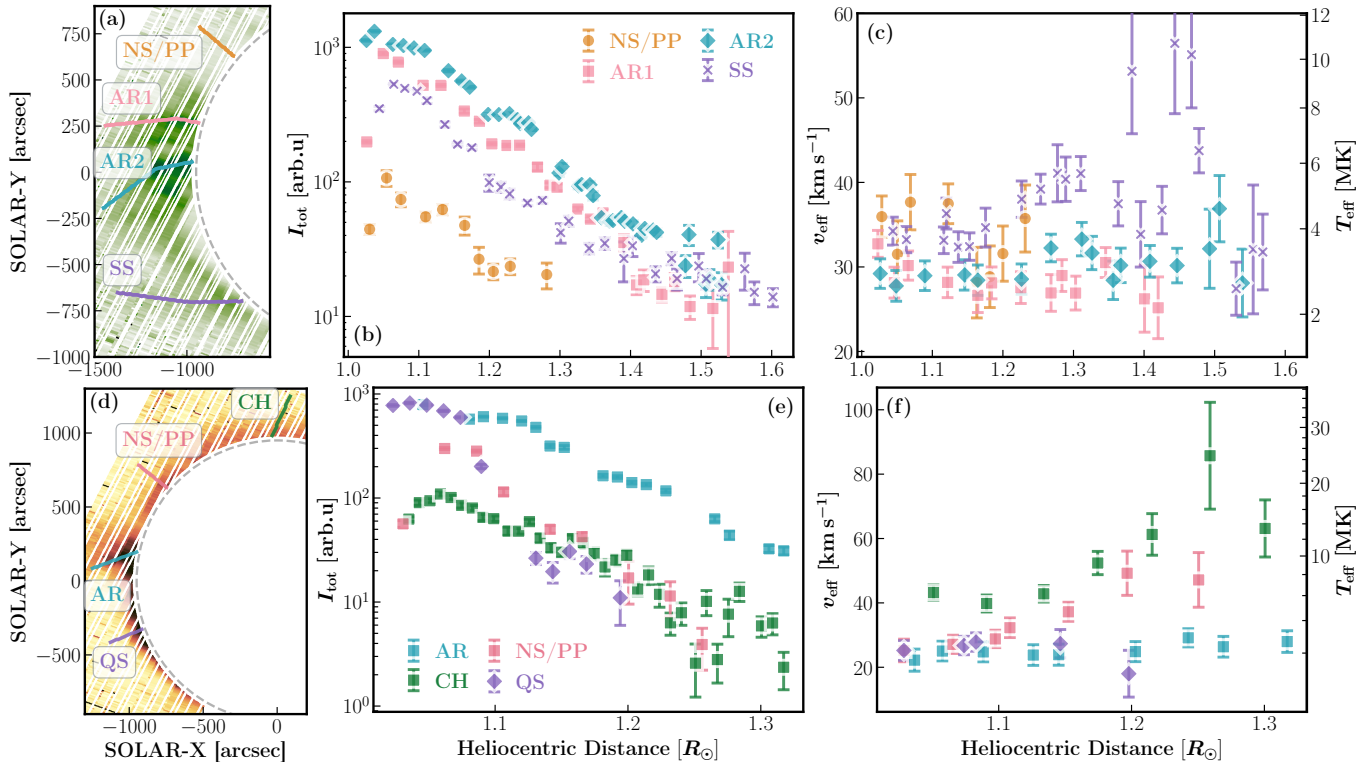
3.1. Hinode/EIS

Figure 4. Fe XIV 530.3 nm line intensity I_{tot} (b) and line width (c) variation along four cuts: northern streamer and polar plumes (NS/PP), active region 1 (AR1), active region 2 (AR2), and southern streamer (SS). Fe X 637.4 nm line intensity I_{tot} (e) and line width (f) variation along four cuts: northern streamer and polar plumes (NS/PP), the coronal hole (CH), the active region (AR), and the quiet Sun (QS). Link to the `Jupyter` notebook creating this figure: ⟲.

3.1.1. Overview and Data Reduction

Although Hinode/EIS did not acquire observations during totality, we compared the 3PAMIS observations with two EIS observations from August 21. One observation (`dhb_polar_scan`) was a raster scan of the north pole CH region, while the other (`Atlas_30`) was a QS observation with a limited FOV at the east limb as shown in Figure 1.

The first CH observation was conducted from 11:08:18 to 14:44:03 UT using the 2″ slit. EIS made a 180-step raster scan with a step size of 2″, resulting in a FOV of 360″×512″. The exposure time of each raster was 70 s. The center of the Fe XII 19.51 nm FOV was 308.4″, 920.9″in the helioprojective Cartesian coordinate.

In the second observation, EIS made a 60-step raster scan of an off-limb QS region north of NOAA AR 12672 from 20:54:39 to UT 21:25:59 UT. Only 160″ along the 2″ slit were used with a step size of 2″, yielding a FOV of 120″×160″. In each raster, EIS made a full CCD exposure with an exposure time of 30 s. The center pointing of EIS at Fe XII 19.51 nm was (-872.9″, 391.9″).

The EIS level-1 HDF5 files were downloaded from the Naval Research Lab (NRL) website[1] and first processed using the EIS Python Analysis Code (EISPAC)[2]. The EIS pointing was corrected by comparing the Fe XII 19.51 nm intensity with the 19.3 nm broadband images taken by the Atmospheric Imaging Assembly (AIA; Lemen et al. 2012) on board the Solar Dynamics Observatory (SDO; Pesnell et al. 2012).

Both EIS observations experienced data losses and hot pixels caused by the South Atlantic Anomaly (SAA), particularly in the QS observation. In addition, the off-limb signal-to-noise ratio (S/N) was too low to make a convincing fit of the spectral line widths. Therefore, additional data binning was required to increase the S/N. Since EISPAC does not support data binning along the slit, we developed our own codes to correct the slit tilt, average the data, and fit the spectral lines.

3.2. Data Analysis and Results

Figure 5 summarizes the EISPAC fitting results for several prominent spectral lines observed in the CH and

AR data sets. The Fe XII 19.5 nm intensity map clearly outlines the boundary of the CH on the disk. Due to the data loss near the center of the FOV and the low S/N in the off-limb CH region, the EIS line profiles were averaged from three distinct regions between 1.03–1.08 $R_\odot$, 1.08–1.13 $R_\odot$, and 1.13–1.18 $R_\odot$ on the left side of the EIS FOV. Additionally, the 2% on-disk intensity was used to estimate and remove the stray light in the off-limb CH (Ugarte-Urra 2010).

In the QS data set, data loss and the hot pixels caused by SAA were identified at the center of FOV. Similarly, two regions were chosen, one spanning 1.035 to 1.06 $R_\odot$ and the other between 1.06 and 1.1 $R_\odot$, to average the EIS data. As the QS region is located close to the limb where the stray light intensity is negligible, and only a few rasters recorded the uncontaminated on-disk spectrum, no stray light correction was applied to the QS data.
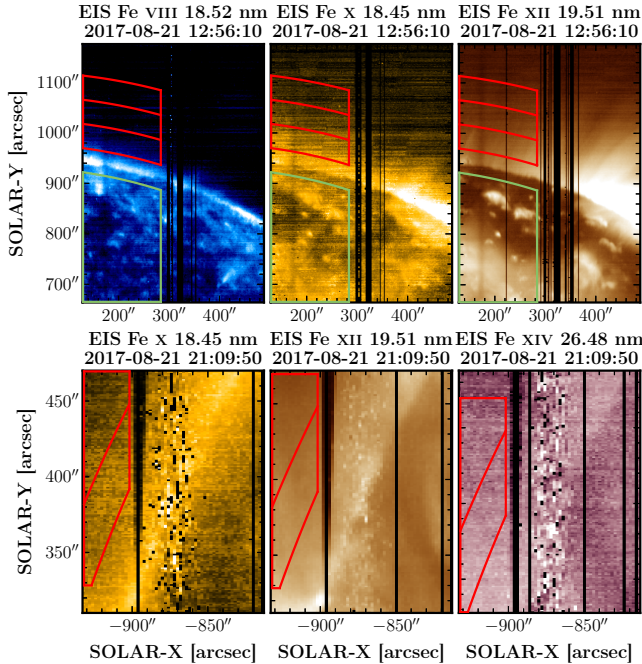
Figure 5. Overview of EIS line intensity fitted by EIS-PAC. Top: `dhb_polar_scan` observation of the CH. Bottom: `Atlas_30` observation of the east limb QS region. The red curves highlight the regions where line profiles are averaged. Profiles in the green boxes are averaged to estimate the off-limb stray light for the CH observation. Link to the `Jupyter` notebook creating this figure: ↻.

Figure 6 illustrates the relationship between $T_{\rm eff}$ and ion charge-to-mass ratio Z/A of different Fe charge states observed by EIS and 3PAMIS in the off-limb CH. To measure $T_{\rm eff}$, the strongest and unblended lines were selected, including the Fe VIII 18.52 nm, Fe X 18.4 nm,

Fe XI 18.82 nm, Fe XII 19.35 nm, and Fe XIII 20.20 nm lines. The coolest Fe VIII 18.52 nm line was only fitted between 1.03–1.08 $R_\odot$ due to S/N limitations. Furthermore, the Fe X 637.4 nm line widths in the same regions are averaged for comparison.

The dependence of $T_{\rm eff}$ on ion Z/A, as observed by EIS, varies at different heights. Between 1.03–1.08 $R_\odot$, Fe VIII, which has the lowest Z/A, shows the highest $T_{\rm eff} \approx 6$ MK. The $T_{\rm eff}$ of the other ions gradually decreases from 4 MK to 3 MK as Z/A increases from 0.16 to 0.22. The decrease in $T_{\rm eff}$ for ions with $0.16 < Z/A < 0.22$ becomes more prominent at 1.08–1.13 $R_\odot$, ranging from more than 6 MK to 2 MK. At 1.13–1.18 $R_\odot$, $T_{\rm eff}$ first drops from about 7.5 MK to 3 MK at $Z/A \sim 0.18$, then gradually increases to 7 MK at $Z/A \sim 0.22$.

The Fe X 637.4 nm line width observed by 3PAMIS agrees with the Fe X 18.4 nm line width observed by EIS at 1.03–1.08 and 1.13–1.18 $R_\odot$. Nevertheless, between 1.08 and 1.13 $R_\odot$, the Fe X 18.4 nm line appears to be much broader than the Fe X 637.4 nm line observed by 3PAMIS, which might be caused by the low S/N and hot pixels in EIS data set. Additionally, it should be noted that the averaging of line profiles in different rasters may include additional orbital drifts not removed by the EIS software (Kamio et al. 2019).

Figure 7 shows the $T_{\rm eff}$ measured by EIS in the QS region, along with a comparison with 3PAMIS results. Benefitting from the full CCD readout and higher S/N, more EIS lines from different ions are utilized, including the Fe IX 19.7 nm, Fe XIV 26.4 nm, Fe XV 28.4 nm, S X 26.4 nm, and Si X 25.8 nm lines. The EIS line widths in the two regions exhibit similarities, while $T_{\rm eff}$ at 1.06–1.1 $R_\odot$ shows a broader distribution, likely due to the lower S/N.

Between 1.035 and 1.06 $R_\odot$, $T_{\rm eff}$ for most ions observed by EIS range from 2–3 MK. Notably, the Fe VIII and Fe IX with the lowest Z/A display slightly higher temperatures compared to the other ions. However, $T_{\rm eff}$ does not show a distinct variation with respect to Z/A in the QS data set, which precludes support for the hypothesis of preferential heating of heavy ions in the QS region at 1.035–1.1 $R_\odot$. Yet, the $T_{\rm eff}$ values for of Fe X and Fe XIV, measured independently by EIS in EUV and 3PAMIS in the visible, are consistent with each other.

EIS observations provide additional plasma diagnostics, including the electron density n_e and electron temperature T_e. Table 1 presents the measured n_e and T_e for the two QS regions, employing three different onboard radiometric corrections reported by Del Zanna (2013, ,GDZ), Warren et al. (2014, HPW), and the latest Del Zanna et al. (2023). The Fe XI and Fe XII diagnostics results using the latest radiometric corrections are quite
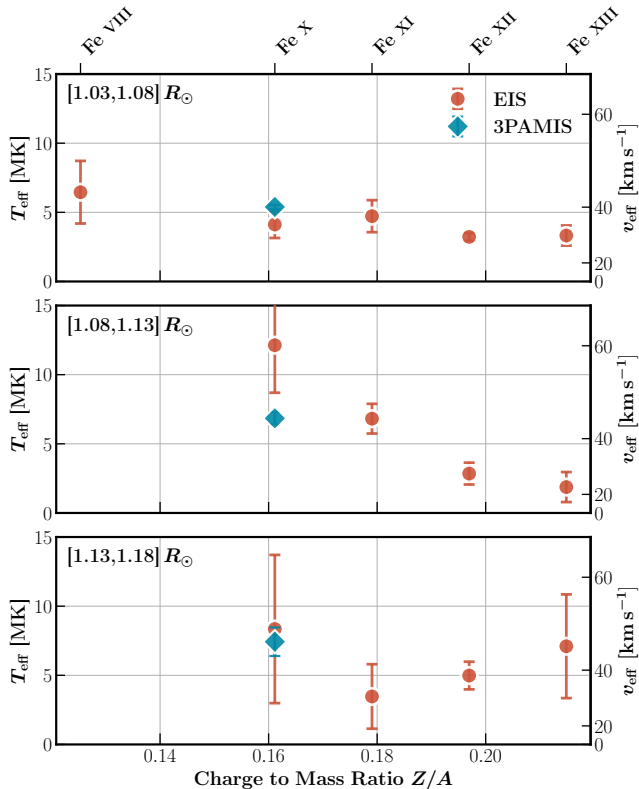
Figure 6. Effective temperature T_{eff} and effective velocity v_{eff} of different ions observed by 3PAMIS and EIS in the north pole coronal hole at three different heights: 1.03–1.08 $R_{\odot}$ (top), 1.08–1.13 $R_{\odot}$ (mid), and 1.13–1.18 $R_{\odot}$ (bottom). Link to the `Jupyter` notebook creating this figure: ☊.
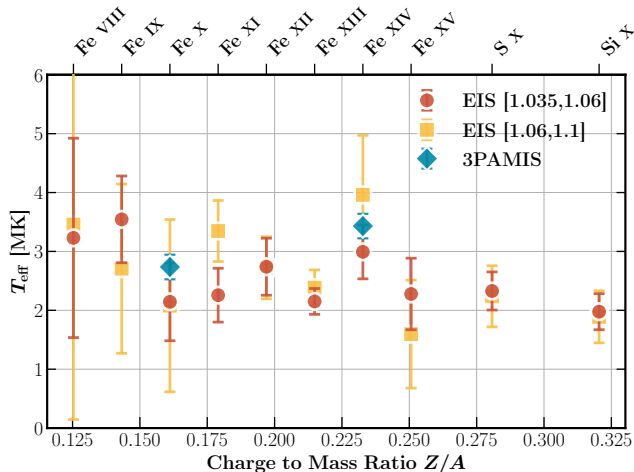

Figure 7. Effective temperature T_{eff} of different ions observed by 3PAMIS and EIS in the off-limb QS region. Link to the `Jupyter` notebook creating this figure: ☊.

different from the other two, which is probably due to the correction of the wavelength-dependent degradation of the detectors after 2012. Notably, the new EIS ra-

diometric calibration is still under review, so we focused on the results using the first two corrections. Besides, density diagnostics using Si x ratios between 1.06 and 1.1 $R_{\odot}$ show great uncertainties due to the low S/N.

Both regions show typical QS n_e and T_e (e.g., Laming et al. 1997; Kamio & Mariska 2012; Feldman et al. 1999; Brooks et al. 2009). In Fe xii, n_e drops from 2.0×10^8 cm^{-3} to 1.5×10^8 cm^{-3}, while T_e increases from 1.2 MK to 1.5 MK in Fe xi. The HPW and GDZ methods yield similar diagnostic results for Fe xii. However, the HPW method provides a higher T_e using Fe xi than the GDZ method. Additionally, n_e inferred from the Si x 25.8/26.1 ratio is much lower if the HPW method is used, amounting to about 50–60% of the GDZ values.

Consistent with numerous other observations (e.g., Hassler et al. 1990; Seely et al. 1997; Banerjee et al. 1998), T_{eff} derived from the line widths were found to be higher than T_e. This implies the existence of unresolved nonthermal motions in both QS and CHs. Assuming $T_i \approx T_e$ in the QS region, we estimate a nonthermal velocity of approximately 15–25 km s^{-1} for ions with T_{eff}=2–3 MK. Additionally, the Z/A dependence of T_{eff} in the CH suggests preferential heating of heavy ions at the base of polar CHs.

n_e (10^8 cm^{-3})					
Ion	Line	Region	GDZ	HPW	New
Si x	25.8/26.1	1	$2.00^{+0.57}_{-0.55}$	$1.35^{+0.47}_{-0.44}$	$2.00^{+0.63}_{-0.49}$
Si x	25.8/26.1	2	$0.91^{+0.56}_{-0.49}$	$\mathbf{0.45^{+0.91}_{-0.45}}$	$1.05^{+0.53}_{-0.50}$
Fe xii	18.6/19.3	1	$2.09^{+0.10}_{-0.09}$	$2.00^{+0.09}_{-0.09}$	$1.45^{+0.03}_{-0.07}$
Fe xii	18.6/19.3	2	$1.58^{+0.16}_{-0.10}$	$1.51^{+0.15}_{-0.10}$	$1.12^{+0.08}_{-0.10}$
T_e (10^6 K)					
Fe xi	18.8/25.7	1	$1.20^{+0.15}_{-0.13}$	$1.51^{+0.19}_{-0.16}$	$2.19^{+0.26}_{-0.28}$
Fe xi	18.8/25.7	2	$1.48^{+0.43}_{-0.38}$	$1.86^{+0.59}_{-0.54}$	> 1.95

Table 1. Electron density n_e and electron temperature T_e diagnostics of regions 1 (1.035–1.06 $R_{\odot}$) and 2 (1.06–1.1 $R_{\odot}$). Fe xii 18.68 nm and Fe xi 25.75 nm lines are self-blended. Entries in the GDZ, HPW, and New columns utilize the radiometric corrections reported by Del Zanna (2013), Warren et al. (2014), and the latest Del Zanna et al. (2023), respectively.

3.3. *CoMP*

CoMP is a tunable coronagraph located at the Mauna Loa Solar Observatory (MLSO). CoMP can perform spectropolarimetric observations of Fe xiii 1074.7 and 1079.8 nm lines in the near-infrared between 1.05–1.35 $R_{\odot}$. The Stokes parameters I, Q, U, and V are

sampled at 3 or 5 wavelength positions across the Fe XIII profiles using Lyot filters. The three-point Stokes I profiles are inverted analytically to obtain the line intensity, Doppler shifts, and widths (Tian et al. 2013). During the 2017 August 21 TSE, CoMP carried out observations from 17:05 to 18:19 UT. We utilized the median Doppler velocity at the east limb as the zero point velocity. An instrumental width of $21\,\mathrm{km\,s^{-1}}$ was removed during the data reduction (Morton et al. 2015).

The inverted Doppler velocities and line widths from the CoMP average file are compared to 3PAMIS observations in Figure 8. The comparison is focused on the Fe XIV line widths and Doppler velocity, given the proximity of this emission line to the formation temperature of Fe XIII observed by CoMP. To make a fair comparison, the CoMP values were resampled at the same pixel scales as 3PAMIS by box averaging and compared with 3PAMIS values using 2D histograms.

The northern streamer is dominated by a redshift of approximately $10\,\mathrm{km\,s^{-1}}$, found to be in agreement with 3PAMIS observations. The equatorial AR, on the other hand, shows no significant Doppler shifts greater than $5\,\mathrm{km\,s^{-1}}$, which slightly differs from the tiny redshifts in 3PAMIS observations. In the southern streamers, blueshifts ranging from 5 to $10\,\mathrm{km\,s^{-1}}$ were found in CoMP observations, slightly greater than 3PAMIS values. In addition, some minor redshifts of less than $2\,\mathrm{km\,s^{-1}}$ were observed at the bottom of the FOV. The 2D histogram reveals some correlation between the Doppler velocity measured by CoMP and 3PAMIS, with a Pearson correlation coefficient of 0.41. However, no significant systematic Doppler shifts $> 2\,\mathrm{km\,s^{-1}}$ were found between the 3PAMIS and CoMP observations. Most differences in Doppler shifts are within the uncertainty of $5\,\mathrm{km\,s^{-1}}$ in the 3PAMIS absolute wavelength calibration.

The line widths observed by CoMP and 3PAMIS also reveal a high level of agreement. The line widths obtained by CoMP are narrower in the equatorial regions, corresponding to $T_{\mathrm{eff}} \approx 3\,\mathrm{MK}$. In contrast, broader line profiles ($T_{\mathrm{eff}} > 4\,\mathrm{MK}$) were found in the northern and southern streamers. The 2D histogram confirmed a good correlation between v_{eff} observed by CoMP and 3PAMIS from 25–$35\,\mathrm{km\,s^{-1}}$, predominantly from the equatorial AR and the streamer structures in the vicinity. Notably, in the data bins with a count of more than 5, CoMP widths were found to be 1–$3\,\mathrm{km\,s^{-1}}$ (approximately 5–10%) greater than the widths observed by 3PAMIS.

3.4. *Comparison with Other Observations*

Koutchmy et al. (2019, hereafter K19) performed a slit spectroscopic experiment during the 2017 TSE and recorded coronal deep spectra from $510\,\mathrm{nm}$ to $590\,\mathrm{nm}$ at six different positions. Fortunately, two positions (Positions 1 and 4) were at the east limb, overlapping with the FOV of 3PAMIS. Fe XIV line widths along these two positions, as digitized from Figures 8 and 9 of K19, are compared with 3PAMIS observations in Figure 9. Position 1 passes the AR and southern streamer, while Position 4 only covers the southern streamer.

Overall, the Fe XIV line widths v_{eff} observed by 3PAMIS were found to be approximately 40% greater compared to those reported by K19. However, 3PAMIS and K19 revealed similar trends in the variation of line widths. Along Position 1 (AR), 3PAMIS observed a relatively constant $T_{\mathrm{eff}} \approx 3\,\mathrm{MK}$, while K19 found a lower $T_{\mathrm{eff}} \approx 1.6\,\mathrm{MK}$. In the southern streamer, both 3PAMIS and K19 exhibited an increase in Fe XIV line widths with height. In 3PAMIS observations, Fe XIV T_{eff} increased slightly from approximately 3 to $4\,\mathrm{MK}$ between 1.1–$1.3\,R_\odot$. On the other hand, T_{eff} in K19 decreased from 3 to $1.5\,\mathrm{MK}$ between 1.0 and $1.15\,R_\odot$, followed by a gradual increase to $3.5\,\mathrm{MK}$ at $1.6\,R_\odot$. The differences between the 3PAMIS and K19 could be attributed to the uncertainty in instrumental widths and/or uncertainty in the coalignment between the two instruments.

4. DISCUSSION

4.1. *Line Widths and Their Variation with Height: Open and Closed Fields*

The Fe X and Fe XIV line profiles observed by 3PAMIS during the 2017 TSE reveal substantial line width variations within and between different structures, especially between the open and closed field regions. In the open fields, line widths are observed to be broader and to increase with height below $1.3\,R_\odot$, while the line widths in closed fields appear to be narrower and nearly constant.

In Figure 10, we compared the observed line widths in different open- and closed-field regions during the TSE with the observed line widths reported by a great number of previous studies. These studies used UV or visible emission lines with similar formation temperatures to Fe X and Fe XIV. The lithium-like ions are also labeled because they usually have high-temperature tails in the equilibrium charge state population. Notably, the absolute magnitudes of v_{eff} are not necessarily the same because of different ion masses and plasma conditions.

The line width variations observed by 3PAMIS are in general agreement with previous studies using UV and visible observations, which reveal minor variations in the closed fields and an increase in the open fields. For instance, a similar increase-then-decrease of Fe XIV widths in streamers was also reported by Mierla et al. (2008).
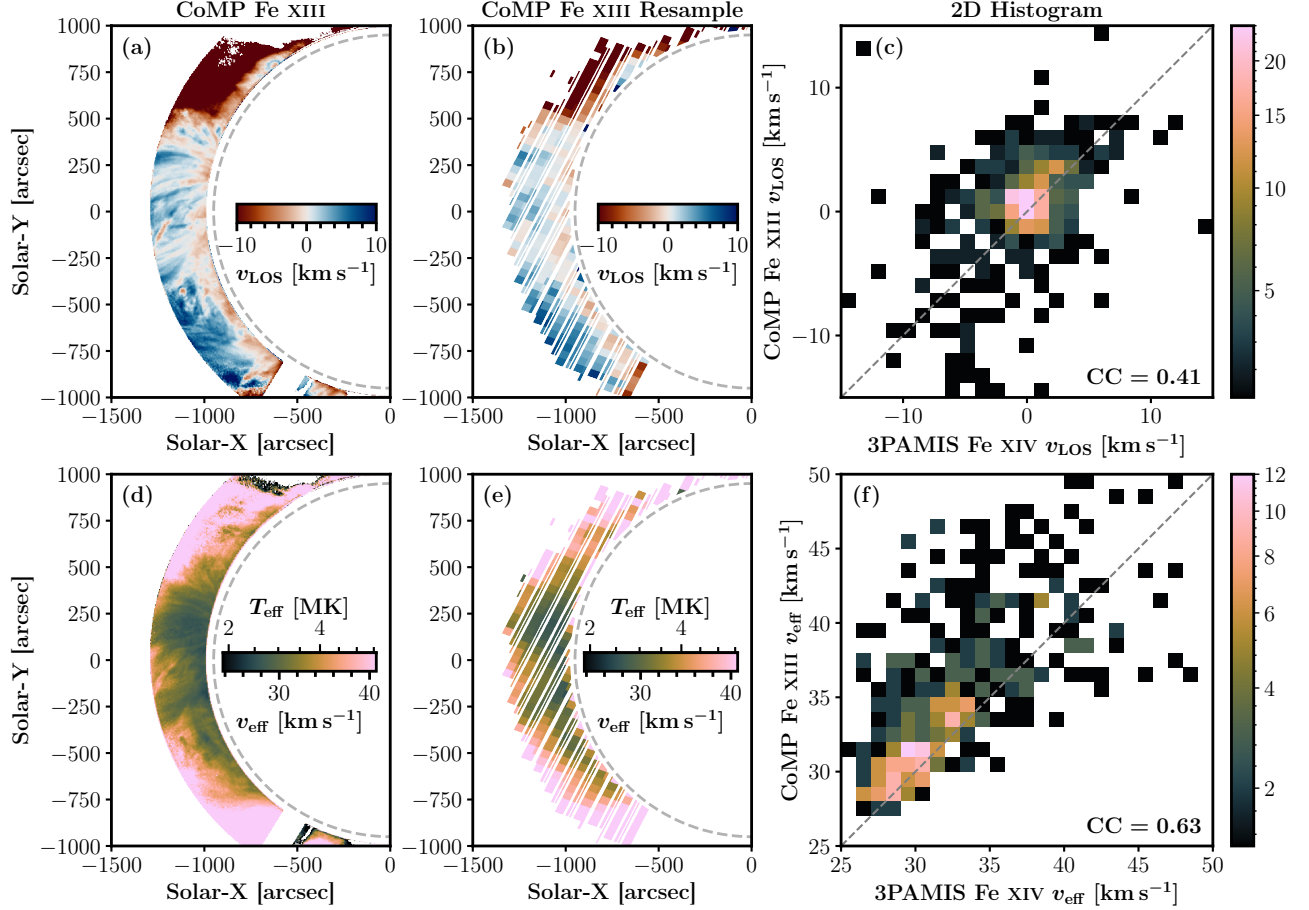
Figure 8. Comparison between the Doppler velocity $v_{\rm LOS}$ and line width observed in Fe XIII 1074.7 nm by CoMP and Fe XIV 530.3 nm by 3PAMIS. (a) CoMP Doppler velocity. (b) CoMP Doppler velocity resampled to match the 3PAMIS pixels. (c) 2D histogram and Pearson correlation coefficient of the Doppler velocity measured by 3PAMIS and CoMP. (d) CoMP Fe XIII line widths. (e) CoMP widths resampled at 3PAMIS pixels. (f) 2D histogram and Pearson correlation coefficient of the widths measured by 3PAMIS and CoMP. Link to the `Jupyter` notebook creating this figure: ⌂.

To effectively address the differences in line widths across various structures or heights, we need to consider both changes in the local parameters, such as ion temperature and nonthermal velocity, and the potential influence of radiative processes on the line width. These processes may include the integration of emission with divergent Doppler shifts along the LOS, nonequilibrium ionization, photoexcitation, and resonant scattering (Gilly & Cranmer 2020).

We chose not to delve into the nonequilibrium ionization in this paper for two primary reasons. First, it requires comprehensive modeling of the coronal and solar wind plasma, which is beyond the scope of this work. Second, the nonequilibrium ionization does not directly affect the widths of local emissivity, while it potentially modifies the profiles through the LOS integration.

4.1.1. *Photoexcitation and Resonant Scattering*

As the height increases and density decreases, photoexcitation and resonant scattering become increasingly important. The visible forbidden lines are photoexcited by the white light continuum emission from the photosphere. Except for the Fe I 530.23 nm line at the blue wing of Fe XIV 530.3 nm, the continuum has no other features and does vary significantly across the profile. Therefore, for Case I scattering between two sharp levels, the Gaussian-like photon redistribution function will convolve with the nearly flat continuum, resulting in a Gaussian emissivity profile. The width of the Gaussian emissivity is still determined by $v_{\rm eff}$, as explained in Appendix B. This is in contrast to the strong UV lines (e.g., Mg X, O VI, and Lyα), as they could be photoexcited by their own profiles from the disk, affecting the width of the local emissivity profile.

Although photoexcitation does not directly alter the widths of local emissivity, it might affect the emissivity from various structures integrated along the LOS. We es-
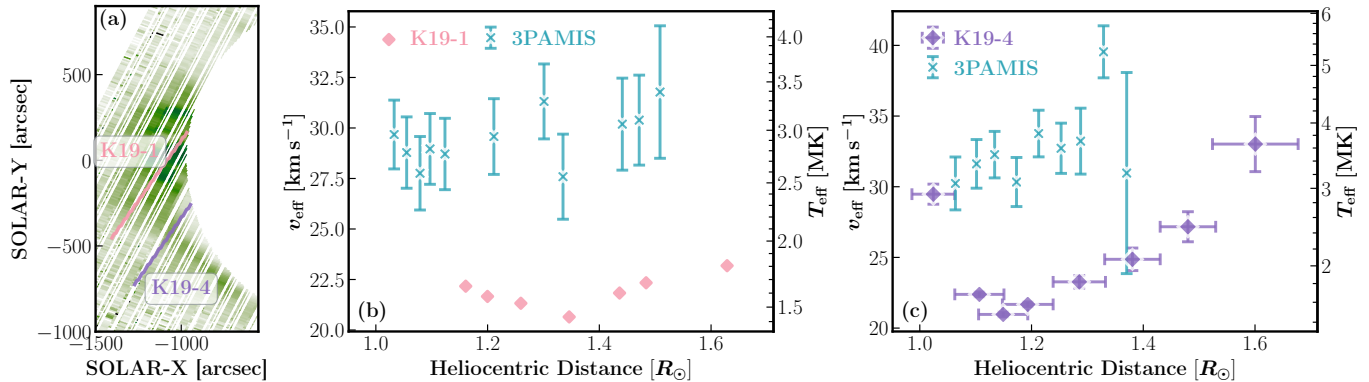
Figure 9. Comparison between the Fe XIV 530.3 nm line widths given as effective velocity $v_{\rm eff}$ in (b) and effective temperature $T_{\rm eff}$ (c) measured by Koutchmy et al. (2019) (red) and 3PAMIS along the slit position 1 (K19-1) and 4 (K19-4) shown in panel (a). Koutchmy et al. (2019) (blue, purple). Link to the `Jupyter` notebook creating this figure: ⊙.

timated the contribution of photoexcitation to populate the upper energy level of Fe XIV in Figure 11, using the electron density inferred from Fe XIII 1074/1079 ratios observed by CoMP. The photoexcitation and three other collisional processes are considered, including electron and proton collisions and radiative decay from higher, collisionally-populated levels. Due to the limitation of the CoMP FOV and S/N, we extrapolated n_e to 1.5 $R_\odot$, assuming an exponential decrease. In the AR at 1.5 $R_\odot$, where $\log n_e \approx 7.3$, photoexcitation only contributes a maximum of 40% of the population. In the streamer, the photoexcitation dominates the level population where $\log n_e$ drops to 7.0 at 1.5 $R_\odot$. Therefore, we suggest that the photoexcitation and resonant scattering may neither significantly influence the line broadening, nor account for the observed discrepancies in line widths between the open and closed fields below 1.2 $R_\odot$, in agreement with early studies by Raju et al. (1991). Quantitative investigations on the influence of photoexcitation and resonant scattering on line broadening above 1.3 $R_\odot$ necessitates a comparison between these observations and global MHD simulations (e.g., the Alfvén Wave Solar Model; van der Holst et al. 2014), which is outside the purview of the study.

4.1.2. *LOS Integration*

Emission originating from multiple structures with various macroscopic Doppler velocities or line widths can contribute to the integral along the LOS in the optically thin plasma. This effect might be evident in open-field structures where fast outflows in the lower corona are expected. Consequently, different Doppler shifts along the LOS may broaden profiles in open-field structures (e.g., Akinari 2007; Zhu et al. 2023).

On the other hand, the relatively constant line width in closed-field structures suggests that the integration of multiple structures along the LOS might not play an important role in the broadening of closed-field profiles. This implication is also supported by the fact that the $v_{\rm eff}$ of approximately 25 km s^{-1} measured in a single AR loop (Gupta et al. 2019) is quite similar to the Fe X $v_{\rm eff}$ obtained by 3PAMIS. If the LOS integration is important, 3PAMIS, with its low spatial resolution, should have observed a larger excess width in the core of AR, where several coronal loops overlap along the LOS, which was not the case.

Gilly & Cranmer (2020) found that a relatively constant line width in the lower corona might be an illusion caused by the LOS integration below the height where the density of the ion charge state reaches its maximum. According to their polar CH and streamer model, they suggested that the Fe X 18.45 nm line width appears constant below 20 Mm, and the width of Si XII, which has a similar formation temperature to Fe XIV, remains constant below 200 Mm. In contrast, during the eclipse, we observed constant line widths up to 200 Mm (Fe X) and 350 Mm (Fe XIV) in the AR. Furthermore, the off-limb AR region consists of the hottest and densest plasma near the POS, surrounded by cooler and more tenuous QS regions, which is opposite to the conditions in the polar CHs. Hence, we argue that the constant line widths cannot be solely explained by the plateauing effect proposed by Gilly & Cranmer (2020).

Finally, the open and close-field structures may overlap along the LOS, which makes it more challenging to interpret the behavior of line widths (e.g., Zhu et al. 2021). This often occurs at the boundary of the open and closed-field regions, such as the variation of Fe X widths in the northern stream and polar plumes regions and Fe XIV widths in the southern streamer observed by 3PAMIS (see Figure 4f).
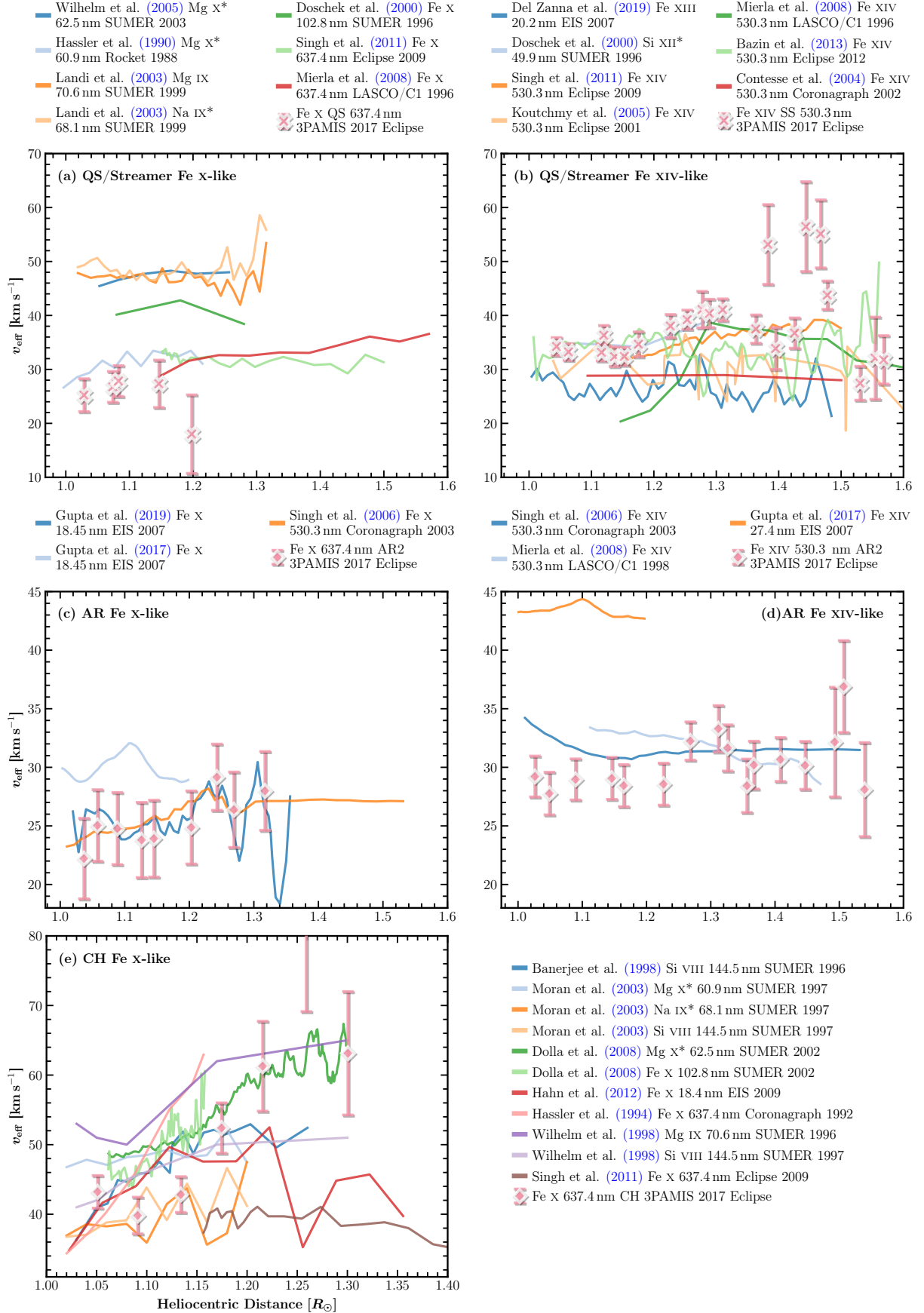
4.1.3. *Preferential Heating*

Figure 10. Comparison of the line widths variation different structures observed by 3PAMIS and other instruments, along with the spectral lines and years of observation. Lithium-like ions are labeled by *. Data is digitized from the listed publications. Link to the `Jupyter` notebook creating this figure: ⭕.
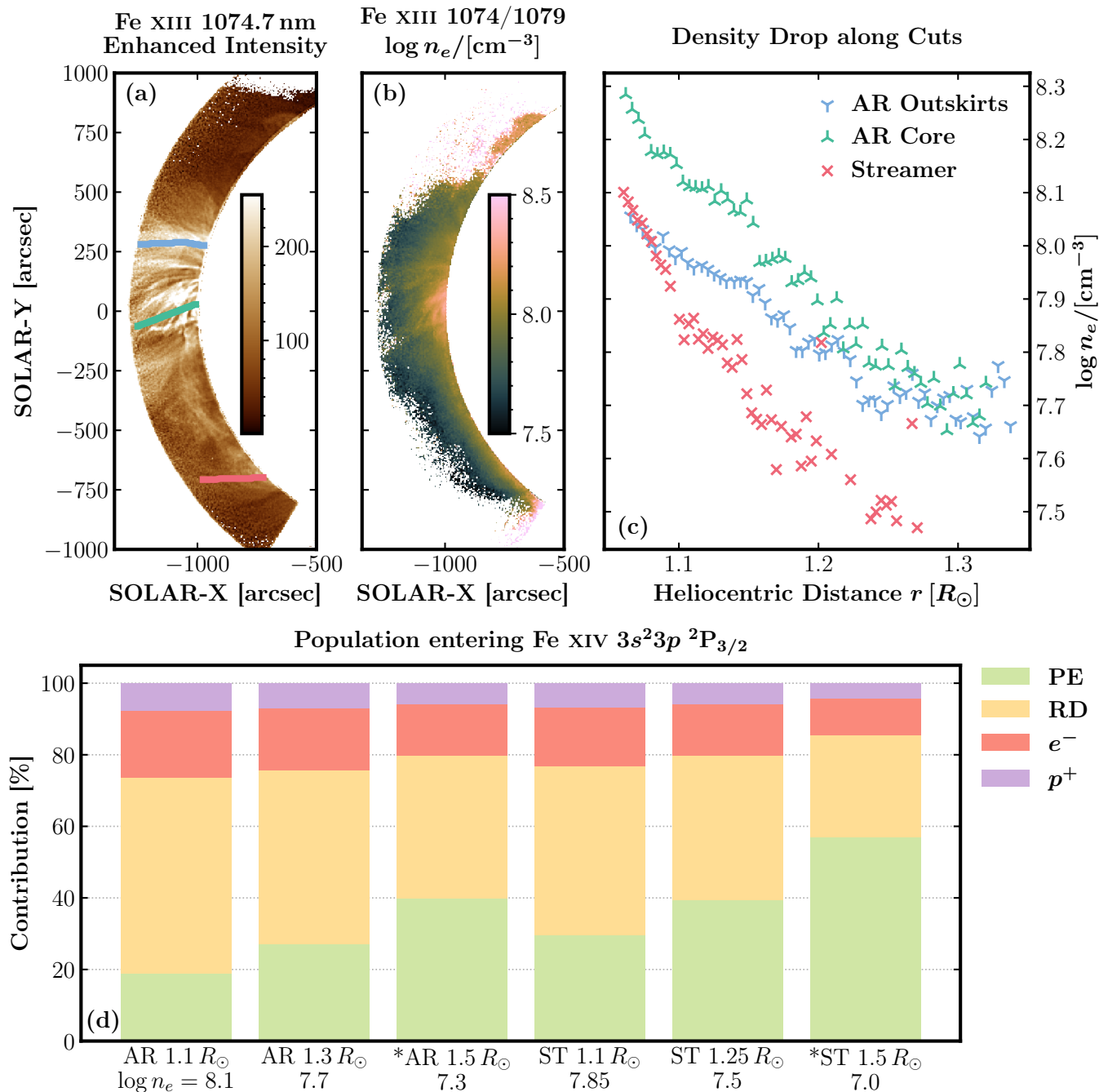
Figure 11. Electron density n_e measured by CoMP and the excitation of the upper energy level of Fe XIV. (a) Fe XIII 1074.7 nm intensity enhanced by a radial intensity filter. (b) Electron density n_e inferred by Fe XIII 1074/1079 ratio. (c) Decrease in n_e along the three cuts shown in Panel a. (d) Population entering the upper energy level of Fe XIV 530.3 nm by different processes at various densities and heights. PE: photoexcitation; RD: radiative decay through cascades from higher levels; e^-: collisions with electrons; p^+: collisions with protons. *n_e is extrapolated, assuming an exponential drop with height. Link to the `Jupyter` notebook creating this figure: ↻.

Low Z/A ions like Fe X are found to be preferentially heated by ion cyclotron waves in CHs, creating excessive thermal broadening (e.g., Tu et al. 1998; Dolla & Solomon 2008; Landi & Cranmer 2009). In this study, the excessive heating to Z/A ions, such as Fe VIII, Fe X, and Fe XI, was also found in the EIS observation of the polar CH. Previous studies reported $T_{\rm eff}$=4–6 MK for Fe X at the base of a polar CH during the solar minimum (Hahn et al. 2010; Zhu et al. 2023), which is consistent with 3PAMIS and EIS observations during the 2017 TSE.

In principle, the constant Fe XIV widths in QS and streamers could potentially be dominated by thermal broadening when nonthermal motions are negligible (Muro et al. 2023). However, this scenario suggests excessive heating of both Fe X and Fe XIV with charge-to-mass ratios (0.16 and 0.23, respectively) in the QS corona.

In contrast to Muro et al. (2023), EIS and 3PAMIS found no evidence of preferential heating in the QS plasma, in agreement with Landi (2007) who studied the QS plasma during solar minimum. In ARs, frequent collisions between ions and electrons can result in $T_i \approx T_e$ (Hara & Ichimoto 1999). This is a common assumption supported by observations (e.g., Imada et al. 2009) and simulations (e.g., Shi et al. 2022).

Incorporated with the assumption of $T_i = T_e$, we used the measurements of T_e made by Boe et al. (2020) during the 2017 TSE to calculate the nonthermal widths of Fe X and Fe XIV in Figure 12. The electron temperatures are inferred by the intensity ratio between Fe XI 789.2 nm and Fe XIV 530.3 nm, which is sensitive to temperatures ranging from 1–2 MK. These two assumptions could introduce uncertainties because (1) T_i may deviate from T_e and (2) Fe XI and Fe XIV emissions may not originate from the same plasma structure along the LOS. The measured T_e in the closed field regions ranges from 1.2 MK to 1.4 MK and does not show significant variations with height. Therefore, the distribution and variation of nonthermal widths in the off-limb corona look similar to that of total line widths. The nonthermal velocity ξ appears to be minimal and constant in the AR, with a value of approximately 15–20 km s^{-1} Fe X ξ exceeds 40 km s^{-1}, suggesting that the assumption $T_i \approx T_e$ might not be valid in these open field regions.

4.1.4. *Wave or Turbulence-induced Nonthermal Motions*

Nonthermal broadening in coronal emission lines has been widely attributed to the propagation of Alfvénic waves, including torsional Alfvén and kink modes, as well as turbulence (e.g., Seely et al. 1997). Essentially, the product of Alfvén wave energy flux and the flux tube cross-section is proportional to $n_e^{1/2}\xi^2$ (Hassler et al. 1990). Therefore, the wave propagation theory particularly favors the increase of line widths in the open fields, as $\xi \propto n_e^{-1/4}$ in the undamped regime (e.g., Dolla & Solomon 2008; Banerjee et al. 2009).

Wave propagation may also result in narrower lines in closed fields. The wave energy flux leaked from the lower atmosphere should be relatively uniform across large scales, particularly in CHs and the QS, where the lower atmospheres are similar. Given $\xi \propto n_e^{-1/4}$, ξ has to be greater in open fields with lower density. Additionally, the nonlinear Alfvén turbulence generated by the counter-propagating waves may dissipate the wave energy more efficiently in closed field regions (van der Holst et al. 2014).

In closed fields, relatively constant line widths may imply wave or turbulence dissipation in the lower corona. For instance, the constant nonthermal width shown in Figure 12, if solely attributed by Alfvén waves, would imply a decrease in the wave energy flux due to the density decrease with height. If the density drops by an order of magnitude from 1.0–1.5 $R_\odot$ in the AR, as shown in Figure 11, the wave energy will decrease by 60–70%. Considering typical values of $\xi \approx 15$ km s^{-1}, $\log n_e \approx 9$, and $B \approx 20$ G at the base of AR, the resulting Alfvén wave energy flux is approximately 10^6 erg cm^{-2} s^{-1}. This energy flux is insufficient to heat AR corona (10^7 erg cm^{-2} s^{-1}, Withbroe & Noyes 1977).

On the other hand, even if the plasma is multithermal along the loop, the constant line width in the AR may still imply the existence of wave damping in ARs. To illustrate this, let's consider a simple case where $v_{\rm eff} \approx 30$ km s^{-1} in Fe XIV is contributed by $T_i = 2$ MK and $\xi = 17$ km s^{-1} at the base of the AR. If the waves are undamped and density drops by an order of magnitude, the new $\xi' = 10^{1/4}\xi \approx 30$ km s^{-1} would dominate the line broadening if $v_{\rm eff}$ remains nearly constant in ARs. Therefore, we should still consider the possibility of wave damping or other nonthermal motions not caused by wave propagation.

4.1.5. *Other Nonthermal Motions*

Despite the fact that the possible wave damping in the closed fields (e.g., Gupta et al. 2019), an alternative explanation to relatively constant line widths is that the nonthermal width ξ in closed fields does not primarily arise from Alfvén waves or turbulence. In fact, a component $\xi_\parallel$ parallel to the magnetic fields is often observed in on-disk ARs (e.g., Brooks & Warren 2016; Prabhakar & Raju 2022), which cannot be simply explained by the Alfvénic waves because the perturbation is perpendicular to the local magnetic field (e.g., Shi et al. 2022). For
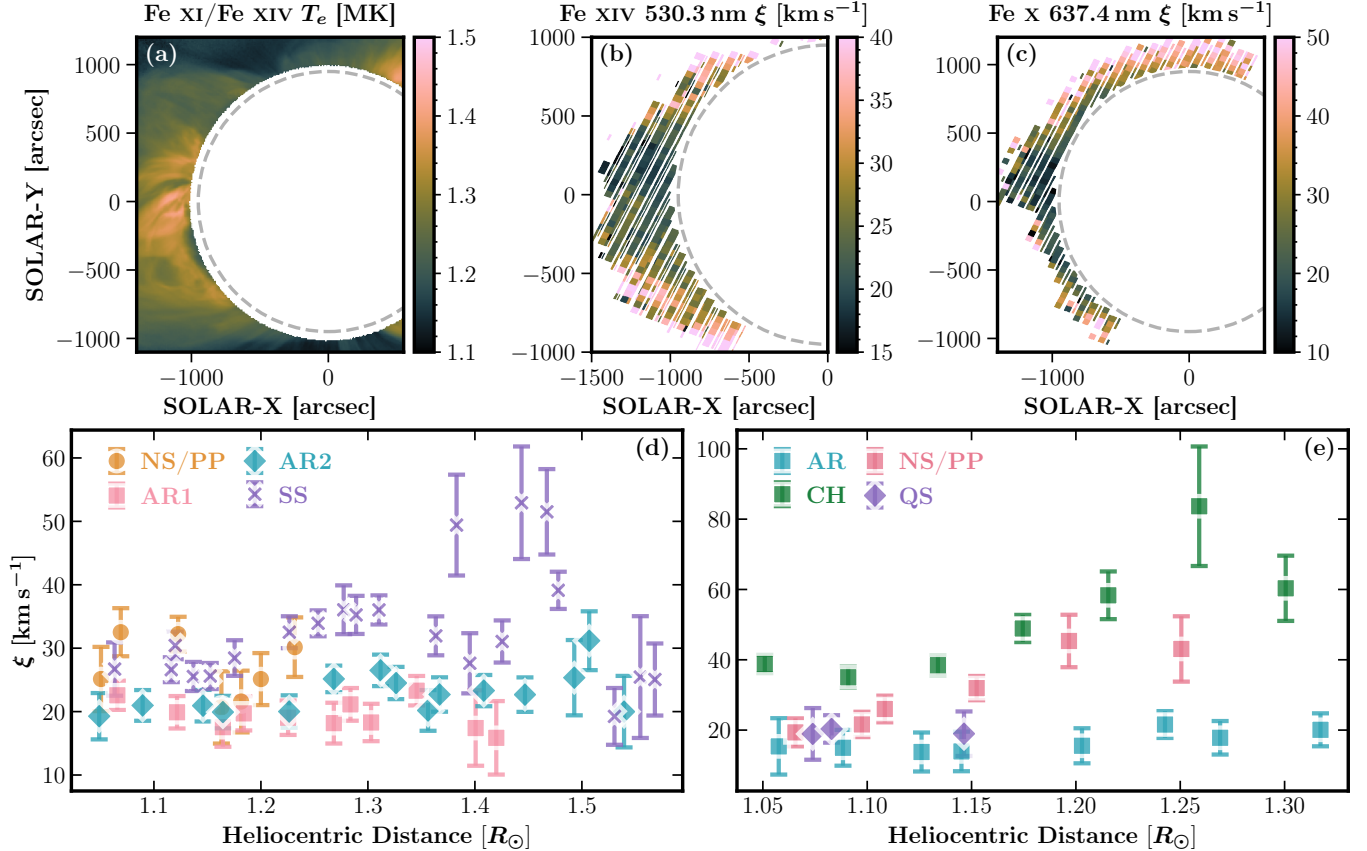
Figure 12. (a) Electron temperature T_e measured by Boe et al. (2020) using the Fe XI 789.2 nm and Fe XIV 530.3 nm ratio. (b) and (c) Nonthermal velocity ξ in Fe XIV 530.3 nm and Fe X 637.4 nm lines. (d) and (e) Nonthermal velocity along the cuts shown in Figure 4. Link to the `Jupyter` notebook creating this figure: ⟳.

example, Asgari-Targhi et al. (2014) had to introduce a parallel component $\xi_\parallel$ with the Alfvén wave turbulence model to reproduce the ξ observed by Hinode/EIS.

A few studies of the anisotropy of the nonthermal velocity confirm the existence of $\xi_\parallel$, but found different relationships between the two components $\xi_\parallel$ and $\xi_\perp$, including $\xi_\parallel > \xi_\perp$ (Hahn et al. 2023) and $\xi_\parallel < \xi_\perp$ (Hara & Ichimoto 1999). The possible candidates to create $\xi_\parallel$ and the relatively constant nonthermal widths in closed fields include reconnection (e.g., jets and nanoflares) or slow mode waves (Hahn et al. 2023), but it is still difficult to reach a firm conclusion (Brooks & Warren 2016).

Additionally, Singh et al. (2002, 2006) proposed that the conduction between the warm and cold plasma within a single coronal loop could lead to a mixture of thermal and nonthermal motions below $1.3\,R_\odot$. This conjecture is supported by observations showing a slight decrease in Fe XIV widths, an increase in Fe X width, and similar line widths between Fe X and Fe XIV from 1.2–$1.3\,R_\odot$ in the AR. Furthermore, other spectroscopic observations have suggested the existence of multi-strand (multi-thermal) loop cross-sections (e.g., Aschwanden

et al. 2013). However, the scenario does not provide a clear explanation for the nature of the nonthermal motions and how they mix with each other within the multi-thermal plasma. A future study using coordinated spectroscopic observations in visible and EUV will provide new insights to explore this scenario.

4.2. Doppler Shifts in the Corona

Significant Doppler shifts greater than $5\,\mathrm{km\,s^{-1}}$ were only observed in Fe XIV 530.3 nm line in the northern and southern streamers, while the Fe X 637.4 nm line does not show any notable Doppler shifts. Interestingly, a redshift of approximately $10\,\mathrm{km\,s^{-1}}$ observed in the northeast region only appeared in Fe XIV, suggesting the presence of bulk motions in the 2 MK plasma. We argue that this redshift results from the plasma motions occurring at the boundary of open and closed-field structures, which is often suggested as the source region of the slow solar wind (e.g., Antiochos et al. 2011). Since the LOS component is approximately $10\,\mathrm{km\,s^{-1}}$, the total outflow velocity may easily exceed $10\,\mathrm{km\,s^{-1}}$. The upcoming 2024 TSE will be another unique opportunity to study the properties of these outflows, as the Solar

Orbiter spacecraft (Müller et al. 2020) will be in quadrature with the Earth during the eclipse. The stereoscopic observations of plasma flows in the lower corona will provide new insights into their source regions and evolution.

5. SUMMARY

We presented spectroscopic observations of the Fe x 637.4 nm and Fe xiv 530.3 nm visible forbidden lines during the 2017 TSE. Benefiting from the large FOV of 3PAMIS with its $4\,R_\odot$ long slit, we analyzed the line intensity, Doppler shifts, and broadening across various corona structures at the east limb up to $1.5\,R_\odot$, including an AR, streamers, and a polar CH. We found distinct behaviors of the line widths between open and closed-field regions. In closed fields, the line widths are narrower, ranging from 20 to $30\,\mathrm{km\,s^{-1}}$, and relatively constant. In contrast, the line widths in open fields are broader ($> 40\,\mathrm{km\,s^{-1}}$) and increase with height between 1.0–$1.3\,R_\odot$.

To complement our observations, we analyzed the observations from Hinode/EIS and CoMP, which provide consistent measurements of the line widths and support our findings. The EIS observations further allow us to measure the widths of other heavy ions in CH and QS regions. We discussed various underlying mechanisms, such as wave propagation, preferential heating, the LOS integration effect, and other nonthermal motions that may affect line widths in open- and closed-field structures. The differences in the width of spectral lines between various coronal structures suggest that wave heating is more dominant in open structures, while localized heating might occur in closed structures.

This study highlights the unique advantages of TSE optical and near-infrared spectroscopy in line width measurements. First, line widths can be obtained at high altitudes with much shorter exposure times compared to conventional EUV spectroscopy. Second, the extended FOV enables simultaneous line width measurements in multiple open- and closed-field regions, providing a comprehensive overview of the global corona. Third, the minimal stray light levels and sky brightness during the totality, complemented by the smaller 3PAMIS instrumental widths, further reduce the uncertainty in measured line widths at great heliocentric distances.

Our study demonstrated the great potential of spectroscopic observations of visible forbidden lines during TSEs in advancing our knowledge of substantial problems, such as coronal heating and solar wind acceleration. For future observations, improvements in the effective area of the spectrograph will empower us to measure Doppler shifts and line widths in the higher corona, for instance, the Fe x width variation above $1.3\,R_\odot$ in CHs. This region was seldom explored by UV observations of lines formed at ~1 MK (see Figure 10e) due to the sharp decrease in line intensity and instrumental stray light. Therefore, it would be of great interest to continue the spectroscopic observations of Fe x 637.4 nm, and other visible forbidden lines during TSEs to shed light on the mysteries of the solar corona.

Software: Numpy (Oliphant 2006; Van Der Walt et al. 2011), Scipy (Virtanen et al. 2020), Astropy (Astropy Collaboration et al. 2013, 2018, 2022), Specutils (Earl et al. 2022), Sunpy (The SunPy Community et al. 2020), EISPAC, Matplotlib (Hunter 2007), CHIANTI (Dere et al. 1997; Del Zanna et al. 2021), SolarSoft (Freeland & Handy 2012), OpenCV (Bradski 2000), num2tex[3], cmcrameri (Crameri 2021), Mathematica, ChatGPT, hissw (Barnes & Chen 2022). The `Jupyter` notebooks and `IDL` scripts for data reduction, analysis, and visualization are available on Zenodo (Zhu et al. 2024) and GitHub.

APPENDIX

A. DATA CALIBRATION AND COALIGNMENT

We performed data reduction and calibration of the raw CCD images through the following steps: (1) dark frame subtraction, (2) curvature correction, and (3) flat-fielding. Furthermore, we determined the instrument pointing, carried out the wavelength calibration, and measured the instrumental broadening of the spectrometer.

We applied dark-frame subtraction to remove both the detector bias and dark current. We created master dark frames for each detector with exposure times of 1 s, 3 s, and 5 s, each obtained by averaging 10 dark frames with the same exposure time, after removing their hot pixels $> 5\sigma$. These master dark frames were subsequently utilized to correct the CCD images with identical or similar exposure times.

In addition, we corrected the curved spectral lines recorded by the detector. The correction of line curvature is crucial for various following calibrations, including flat-fielding, pixel binning along the y-axis, wavelength calibration, and fitting of line widths. To accomplish this, we employed emission from neutral hydrogen and helium calibration lamps in the laboratory to measure the curvature.

The measurement of the curvature was carried out in two steps: (1) We averaged every 5 pixels along the y-axis and fitted the line centroids at different CCD y-pixels using single-Gaussian fitting (see Figure 13b). The shift along the x-axis was measured with respect to the line centroid at $y = 400$. (2) To extrapolate the shift from where calibration lines were located to the entire detector, we utilized a 2-D Chebyshev polynomial. The latter is a first-order polynomial in the x-direction and a second-order polynomial in the y-direction; it was used to fit the shift of all calibration lines at various parts of the detector. This approach was chosen to emulate the legacy Image Reduction and Analysis Facility (IRAF) and its user guide for slit spectroscopy (Massey et al. 1992). Then we interpolated each pixel along the x-axis to correct the curvature (Figure 13c). All the images used in this study, except for the dark frames, were subjected to the curvature correction procedure.

We performed flat-fielding corrections only along the y-direction for several reasons. First, the spectral lines are recorded along the y-axis of the detector. Second, the laboratory/dome flats were not used, as they were acquired when the slit was not evenly illuminated. Finally, the sky flats contain a considerable number of telluric lines (see Figure 14a). To obtain the 1-D flat-fielding function, we averaged the "clean" sky flat images between telluric contamination. We carried out this procedure specifically at the regions of the detector where Fe X and Fe XIV lines were located. Figure 14c illustrates an example of the flat-fielding curve for the Fe X 637.4 nm line at the 52nd order. It is important to note that the 1-D flat-fielding primarily corrects optical effects, such as vignetting, but does not correct the response differences of individual CCD pixels.

We performed the wavelength calibration in two steps: (1) a relative wavelength calibration using laboratory hydrogen and helium calibration lines, followed by (2) an absolute wavelength calibration using chromospheric hydrogen and helium emission at the limb. Figure 15 shows the relative wavelength calibration of the green and red detectors. Specifically, Hβ, He I 501.6 nm, and He I D$_3$ are used for the green detector and Hα, He I D$_3$, and He I 667.8 nm are used for the red detector. The He I D$_3$ line at 587.6 nm can be observed in both detectors because it is close to the wavelength limit of the dichroic mirror. To derive the wavelength scale, we adopted a second-order polynomial to fit the NIST air wavelengths of neutral hydrogen and helium lines. The wavelength scales at the detector center are approximately $0.025\,\mathrm{nm\,px^{-1}}$ (62nd order, green) and $0.030\,\mathrm{nm\,px^{-1}}$ (52nd order, red).

A significant deviation from the laboratory wavelength scale was found in the totality images, likely resulting from slight perturbations of the optics during transportation and deployment. Therefore, we carried out an additional absolute wavelength calibration using chromospheric lines at the limb to correct the reference wavelength.
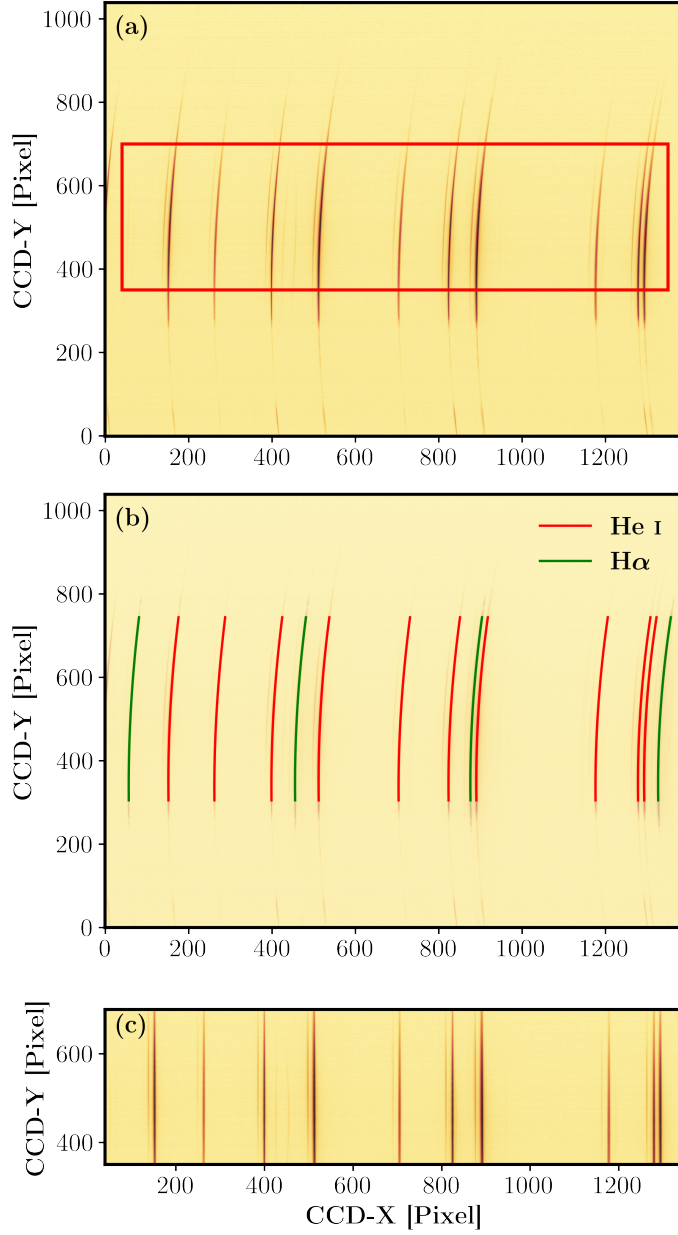
---

[3] https://github.com/AndrewChap/num2tex

Figure 13. An example of curvature correction: (a) A CCD image showing curved neutral helium spectral lines on the detector. The red rectangle outlines the region shown in panel (c) where the curvature is corrected. (b) Fitting of curved neutral hydrogen and helium lines. (c) Curvature-corrected helium lines from the red rectangle in panel (a). Link to the `Jupyter` notebook creating this figure: ⦿.

Figure 16 displays the absolute wavelength calibration of the green detector. We found a shift of approximately 5 pixels along the x-direction between the chromospheric lines and the same lines measured in the laboratory. We utilized the average pixel shift at different orders to update the reference wavelength. The average shifts are found to be -5.56 pixels for the green detector and -1.17 pixels for the red detector. Moreover, the spread of the pixel shift in Figure 16c allowed an estimation of the uncertainty in wavelength calibration, which was about 1/3 pixel (≈ 0.008 nm or 4.5 km s^{-1} at 530 nm). Additionally, we chose the median value of the Doppler shift measured in the FOV as the zero point velocity to remove the solar rotation.

In addition to the wavelength calibration, we adopted the neutral hydrogen and helium lines to measure the instrumental broadening. As the thermal and nonthermal broadening of these calibration lines is negligible, the widths of
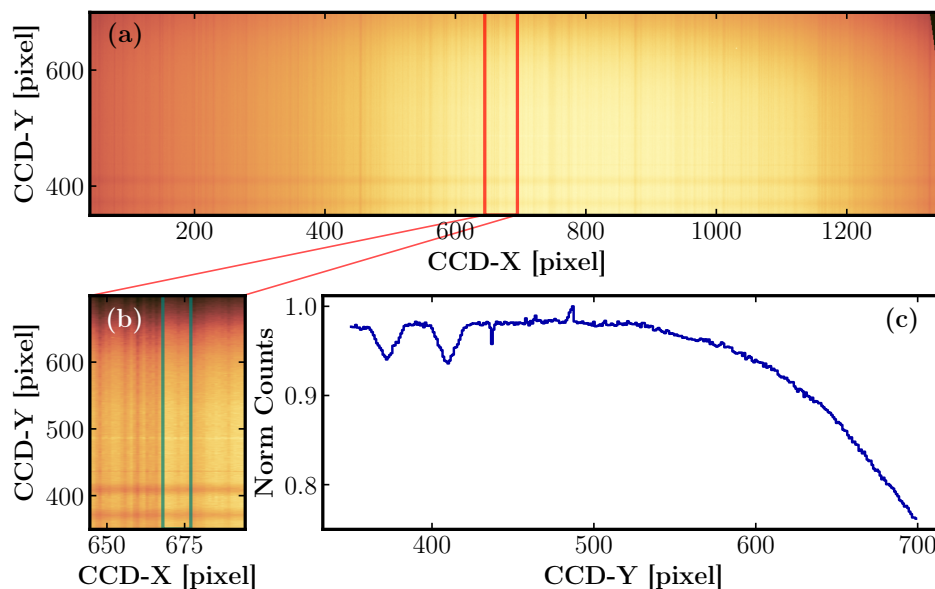
Figure 14. 1-D flat field function of the red detector for 52nd-order Fe x 637.4 nm line. (a) Curvature-corrected sky flat image. (b) Zoom-in sky flat image. (c) The 1-D flatfield function averaged between the two green vertical lines. Link to the `Jupyter` notebook creating this figure: ⟳.
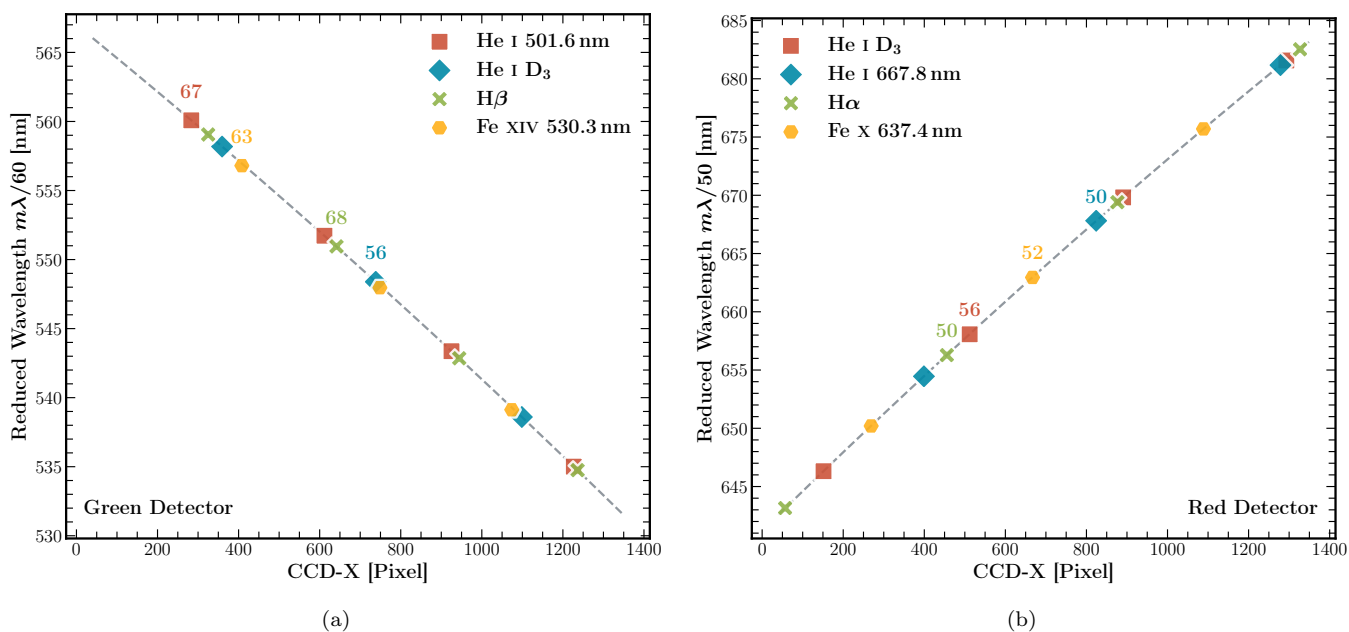
Figure 15. CCD x-pixel positions of various-order spectral lines and the relative wavelength calibration of the green (left) and red (right) detectors. The neutral hydrogen and helium lines are used in the wavelength calibration. The dashed curves show the quadratic fittings of wavelengths. The locations of the observed Fe x and Fe xiv lines during the eclipse are also shown. Links to `Jupyter` notebooks creating this figure: ⟳ (green) and ⟳ (red).

calibration lines provided a direct measurement of the instrument widths. We noticed that the interpolation to correct the line curvature might affect the fitted line widths because the calibration lines are very narrow and usually only sampled by 4-5 pixels in the x-direction.

To address this concern, we compared the curvature-corrected and uncorrected widths as a function of CCD y-pixel in Figure 17. We found that the two line widths agree with each other when the curvature is negligible ($y \approx 400$).
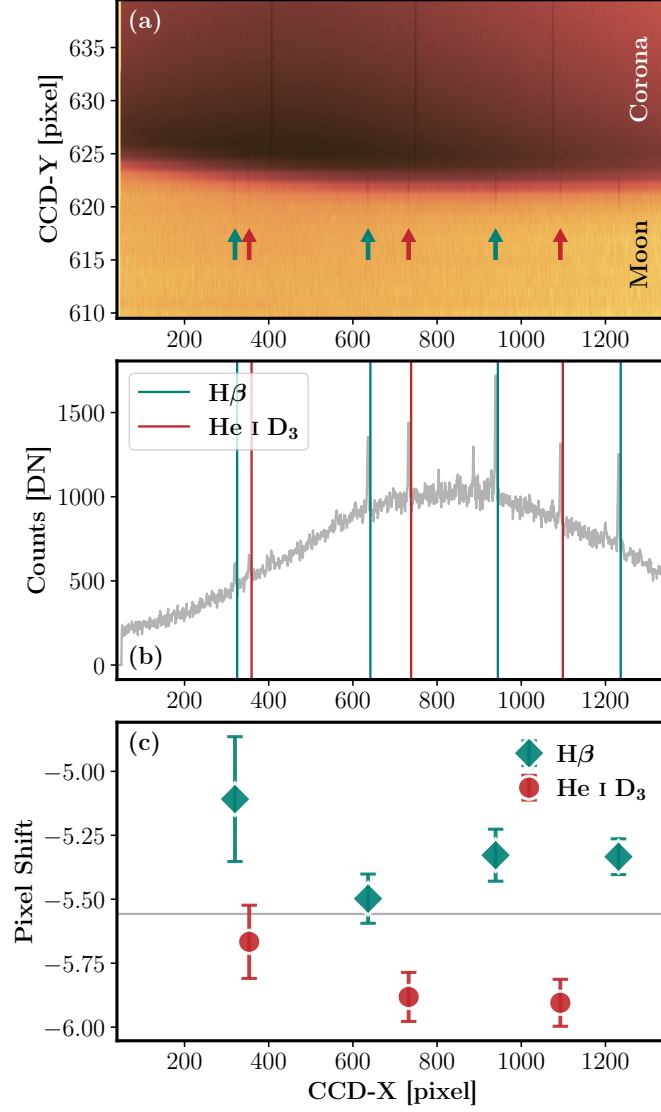
Figure 16. Absolute wavelength calibration of the green detector. (a) Chromospheric Hβ(green arrow) and He I (red arrow) emissions between the lunar disk and corona. (b) The average chromospheric spectrum (grey curve) between the two red ticks in panel (a). The vertical green and red lines indicate the line centroids of laboratory Hβ and He I. (c) The shift between the chromospheric lines and the laboratory lines at different orders. The horizontal grey line indicates the average pixel shift for the absolute wavelength calibration. Link to the `Jupyter` notebook creating this figure: ⌗.

However, at locations where lines are curved, the uncorrected widths fluctuate from 1.4 to 1.9 pixels (green) and 1.5 to 2.1 pixels (red), which might be attributed to the insufficient sampling of the line profile. Notably, the curvature correction failed to remove the fluctuation, particularly for the red detector, where the curvature-corrected widths vary from 1.6 pixels to 2.5 pixels.

Finally, we selected the region where the uncorrected widths do not vary significantly to measure the instrumental widths, at $y \sim 380$ for the green detector and $y \sim 350$ for the red detector. The instrumental widths of $\Delta\lambda_{\mathrm{inst,green}} = 1.86\,\mathrm{px}$ and $\Delta\lambda_{\mathrm{inst,red}} = 2.12\,\mathrm{px}$ are used in this study, with an uncertainty of approximately $20-30\%$. We estimated the uncertainties of instrumental widths as $\sigma_{\mathrm{inst}} = 0.4\,\mathrm{px}$ (green) and $\sigma_{\mathrm{inst}} = 0.5\,\mathrm{px}$ (red), based on the spread of values depicted in Figure 17. The instrumental widths are removed by

$$\Delta\lambda_{\mathrm{true}} = \sqrt{\Delta\lambda_{\mathrm{fit}}^2 - \Delta\lambda_{\mathrm{inst}}^2} \tag{A1}$$

where $\Delta\lambda_{\mathrm{true}}$ is the deduced true line width. We also propagated the uncertainty by

$$\sigma_{\mathrm{true}} = \left(\frac{\lambda_{\mathrm{fit}}^2}{\lambda_{\mathrm{true}}^2}\sigma_{\mathrm{fit}}^2 + \frac{\lambda_{\mathrm{inst}}^2}{\lambda_{\mathrm{true}}^2}\sigma_{\mathrm{inst}}^2 \right)^{1/2} \tag{A2}$$

where σ_{true} is the uncertainty of $\Delta\lambda_{\mathrm{true}}$, σ_{fit} denotes the fitting uncertainty.
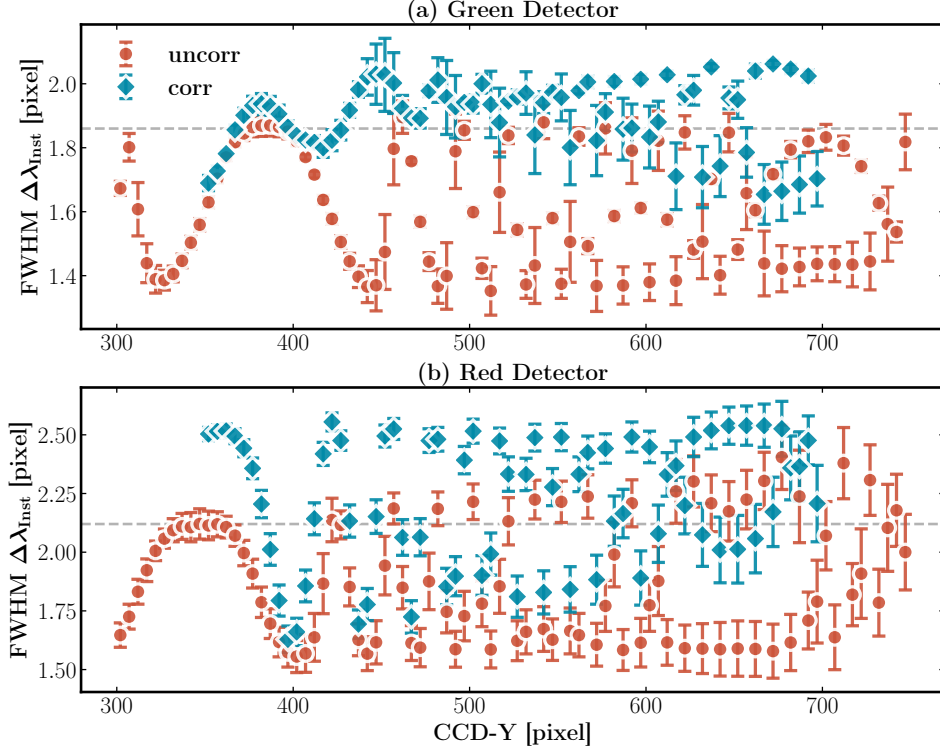
Figure 17. Line widths of the narrow neutral hydrogen and helium lines as a function of CCD y-pixel position in the green (a) and red (b) detectors. The blue diamonds represent the curvature-corrected widths, and the red dots are for the uncorrected widths. The dashed horizontal lines indicate the instrumental widths used in this study. Link to the `Jupyter` notebook creating this figure: ⚙.

Regrettably, the 3PAMIS FITS headers do not include any pointing information since the instrument was set up on-site manually, only a few days prior to the eclipse. Therefore, we had to rely on the white light images taken by the context camera to determine the pointing. Although the context camera did not record the time of observation, this information was available in 3PAMIS FITS headers. Hence, we manually compared the 3PAMIS images taken at the onset of totality with the context images to determine the reference time.

To begin, we determined the slit position relative to the solar disk. As the pointing of the slit was fixed, our task involved measuring the motion of the Sun in the context images. To accomplish this, we adopted the circle Hough Transform method (Duda & Hart 1972) available in OpenCV to detect the lunar limb as a circular feature in the images (see Figure 18a). Subsequently, we performed linear fitting on the x and y-coordinates of the lunar disk when the Sun crossed the slit (Figure 18b and c) to measure the velocities of the Sun $v_{\odot,x}$ and $v_{\odot,y}$. To convert these velocities in pixels into arcsecs, we compared the radius of the lunar disk (approximately 71.4 pixels, see Figure 18d), with the lunar disk size $976''$ reported in Boe et al. (2020).

We took advantage of the semi-transparent slit mirror to measure the spatial scale Δy of the detectors. Figure 18e displays a CCD image captured when the slit was pointed to the off-limb. Two faint horizontal lines can be identified on the image, which are caused by the dispersion of the limb image leaking from the semi-transparent slit mirror. We used the positions of these lines to derive the spatial scale Δy of two detectors and the position of the disk center y_c on the detector. The spatial scales Δy of the two detectors are measured to be $8''.26\,\mathrm{px}^{-1}$ (green) and $8''.37\,\mathrm{px}^{-1}$ (red).
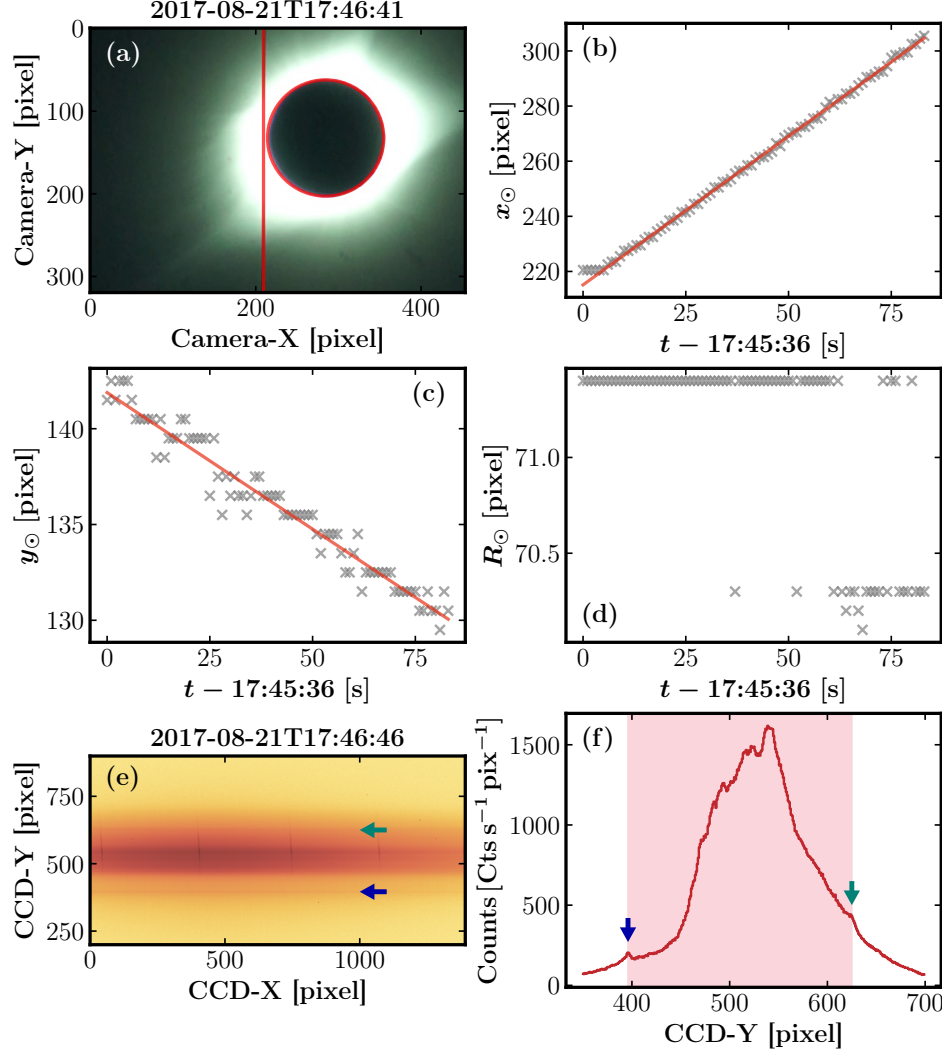
Figure 18. Determining the spectrograph pointing: (a) Fitting the lunar limb on context images. The red cycle highlights the lunar limb, and the red vertical line represents the position of the slit. (b) and (c) Linear fitting of the motion of the disk center on context images. (d) Variation of the fitted disk radius. (e) An off-limb CCD image. The blue and green arrows indicate limb emission leaking from the slit mirror. (f) CCD counts averaged along the x-axis, with the arrows being the same as Panel (e). The shaded pink area between the two arrows is used to calculate the spatial sampling of the detector. Link to the `Jupyter` notebook creating this figure: ⟳.

The final crucial parameter is the angle α between the slit and the solar north–south direction. The slit was slightly tilted from solar northwest to southeast as depicted in Figure 18a. Initially, we compared the locations of streamers in the white light context images with the reference eclipse images from Boe et al. (2020). However, because the inner corona was saturated in the context images, this approach only yielded an angle of approximately $30°$. Therefore, we manually compared the Fe XIV intensity observed by 3PAMIS with Fe XIV narrowband images to obtain a better estimation of the angle $\alpha = 27°5$.

Finally, the transformation from detector pixel at y-pixel y_i taken at time t_i to the helioproject coordinates (θ_x, θ_y) in arcsec is given by

$$
\begin{bmatrix} \theta_x \\ \theta_y \end{bmatrix} = \begin{bmatrix} \cos\alpha & \sin\alpha \\ -\sin\alpha & \cos\alpha \end{bmatrix} \begin{bmatrix} (t_i - t_0)v_{\odot,x} + \theta_{x,0} \\ (y_i - y_c)\Delta y + (t_i - t_0)v_{\odot,y} \end{bmatrix}
\tag{A3}
$$

where $\alpha = 27°\!.5$ is the slit tilting angle. $v_{\odot,x}$ and $v_{\odot,y}$ are the velocities of the Sun in arcsec captured by the context camera. $t_0 =$UT17:46:38 corresponds to the reference time when the slit first pointed to off-limb. $\theta_{x,0}$ denotes the distance between the slit and disk center at t_0 in arcsec. y_c represents the disk center position on the detector at t_0.

It is important to acknowledge that the method used to determine the instrumental pointing has certain limitations. First, the circle Hough Transform method used to detect the lunar limb has a precision of 1/2 pixel, which translates to about $6''\!.7$. Second, the time of observation recorded in the 3PAMIS FITS header has a limited precision of 1 sec. Given that the Sun moved nearly perpendicular to the slit at a speed of about $15''\,\mathrm{s}^{-1}$, an inaccurate time of observation may result in an uncertainty of $\sim 10''$ perpendicular to the slit. Third, the slit tilt angle α determined by comparing Fe XIV intensity with narrowband images cannot achieve better results than the spatial scale of the detector, which is $\sim 8''$. This limitation could be more significant towards the two ends of the slit due to the focus on comparing the features in the AR. Additionally, the rotation of the slit mixes the uncertainty along and perpendicular to the slit. Overall, we estimated that the pointing used in this study might have an uncertainty up to 20–$30''$.

No radiometric calibration was performed due to the lack of laboratory light sources and the multi-order design of the spectrometer. However, we still estimated the uncertainty in each pixel, assuming the photon shot noise follows the Poisson statistics:

$$\sigma_D = \sqrt{D_0 + \sigma_0^2} \tag{A4}$$

where D_0 is the total count in data number (DN) after the dark frame subtraction, and σ_0 is the combination of CCD readout noise and dark current noise estimated from the standard deviation of the master dark frames. We note that σ_D only represents the relative magnitude of the uncertainty in each pixel since the absolute magnitude of the photon shot noise is the square root of the photon counts or photon electron counts. The non-linear least square routine to fit the Gaussian profiles will automatically rescale these uncertainties to reach a unity χ^2.

B. PHOTON REDISTRIBUTIONS OF CONSTANT CONTINUUM

Physically, it is trivial, to some extent, that the flat continuum resonantly scattered by a Gaussian absorption profile leads to another Gaussian profile. To provide a detailed proof in this Section, we consider the local emissivity $\epsilon(\nu, \hat{\boldsymbol{n}})$ at a frequency ν in the direction of $\hat{\boldsymbol{n}}$ caused by the incident emission is proportional to

$$\epsilon(\nu, \hat{\boldsymbol{n}}) \propto \frac{1}{4\pi} \int \mathrm{d}\Omega' \int_0^\infty \mathrm{d}\nu' R(\nu', \hat{\boldsymbol{n}}'; \nu, \hat{\boldsymbol{n}}) I(\nu', \hat{\boldsymbol{n}}') \tag{B5}$$

where the integral over the differential solid angle $\mathrm{d}\Omega'$ describes the scattering of incoming photons from different directions. $R(\nu', \hat{\boldsymbol{n}}'; \nu, \hat{\boldsymbol{n}})$ is the photon redistribution function in the observer's frame, which describes the probability to scatter an incoming photon at frequency ν' and along direction $\hat{\boldsymbol{n}}'$ to a new frequency ν and direction $\hat{\boldsymbol{n}}$, and $I(\nu', \hat{\boldsymbol{n}}')$ is the incoming photospheric radiation intensity. Consider the scattering from a constant (flat) continuum $I(\nu', \hat{\boldsymbol{n}}') = I(\hat{\boldsymbol{n}}')$, we have

$$\epsilon(\nu, \hat{\boldsymbol{n}}) \propto \frac{1}{4\pi} \int I(\hat{\boldsymbol{n}}')\mathrm{d}\Omega' \int_0^\infty \mathrm{d}\nu' R(\nu', \hat{\boldsymbol{n}}'; \nu, \hat{\boldsymbol{n}}) \tag{B6}$$

Let's first deal with the integral over the incident frequency

$$\mathcal{I}_1 = \int_0^\infty R(\nu', \hat{\boldsymbol{n}}'; \nu, \hat{\boldsymbol{n}})\mathrm{d}\nu' \tag{B7}$$

Assuming the scattering happens between two sharp energy levels, neglecting the natural broadening (Case I, Mihalas 1978), the analytical form of the photon redistribution function can be written as (Cranmer 1998; Gilly & Cranmer 2020)

$$R(\nu', \hat{\boldsymbol{n}}'; \nu, \hat{\boldsymbol{n}}) = \frac{g(\Theta)}{\pi\beta(\Delta\nu)^2} \exp\left(-\zeta'^2\right) \exp\left[-\left(\frac{\zeta - \alpha\zeta'}{\beta}\right)^2\right] \tag{B8}$$

where $\Theta = \langle \hat{\boldsymbol{n}}', \hat{\boldsymbol{n}} \rangle$, $\alpha \equiv \cos\Theta$, and $\beta \equiv \sin\Theta$. $g(\Theta)$ is the angular distribution phase function. $\Delta\nu = \nu_0 v_{\mathrm{eff}}/c$ represents the local effective velocity in frequency units, where ν_0 is the rest frequency of the spectral line. Additionally, ζ and

ζ' are dimensionless frequency displacements defined by

$$\zeta \equiv \frac{\nu - \nu_0}{\Delta\nu} - \frac{\boldsymbol{u} \cdot \hat{\boldsymbol{n}}}{v_{\mathrm{eff}}} = \frac{\nu - \nu_0\,(1 + u_{\mathrm{LOS}}/c)}{\Delta\nu} \tag{B9}$$

$$\zeta' \equiv \frac{\nu' - \nu_0}{\Delta\nu} - \frac{\boldsymbol{u} \cdot \hat{\boldsymbol{n}}'}{v_{\mathrm{eff}}} \tag{B10}$$

where $\boldsymbol{u}$ denotes the local bulk velocity and $\boldsymbol{u} \cdot \hat{\boldsymbol{n}}$ is the local LOS velocity u_{LOS}. Replacing $\mathrm{d}\nu'$ with $\Delta\nu\mathrm{d}\zeta'$, the integral in Equation (B7) can be written as

$$\begin{aligned}
\mathcal{I}_1 &= \frac{g(\Theta)}{\pi\beta\Delta\nu} \int_{-\nu_0/\Delta\nu - \boldsymbol{u}\cdot\hat{\boldsymbol{n}}'/v_{\mathrm{eff}}}^{\infty} \exp\left(-\zeta'^2\right) \exp\left[-\left(\frac{\zeta - \alpha\zeta'}{\beta}\right)^2\right] \mathrm{d}\zeta' \\
&\approx \frac{g(\Theta)}{\pi\beta\Delta\nu} \int_{-\infty}^{\infty} \exp\left(-\zeta'^2\right) \exp\left[-\left(\frac{\zeta - \alpha\zeta'}{\beta}\right)^2\right] \mathrm{d}\zeta' \\
&= \frac{g(\Theta)}{\sqrt{\pi}\Delta\nu} \exp\left(-\zeta^2\right)
\end{aligned} \tag{B11}$$

note that we also used $v_0 \gg \Delta\nu$ and $\alpha^2 + \beta^2 = 1$. Notably, $\mathcal{I}_1$ is a Gaussian profile, which does not depend on $\hat{\boldsymbol{n}}'$ anymore. Thus, the local emissivity is

$$\epsilon(\nu, \hat{\boldsymbol{n}}) \propto \frac{\mathcal{I}_1}{4\pi} \int I(\hat{\boldsymbol{n}}')\mathrm{d}\Omega' \tag{B12}$$

where the integral over the solid angle is a scale factor due to the limb darkening. Therefore, the local emissivity is still a Doppler-shifted Gaussian function broadened by the local effective velocity v_{eff}.

C. COMPARISON BETWEEN ORDERS

One of the advantages of 3PAMIS is its capability to work at multiple orders, allowing for measurements of line profiles multiple times. However, in this study, we have only adopted the most prominent order of Fe X and Fe XIV lines. To improve the S/N, a natural approach is to combine line profiles in different orders to make the best use of collected photons.

In Figure 19, we present examples of Fe XIV line profiles at various orders obtained from different off-limb locations. In addition, we interpolated the line profiles at various orders to the same wavelength scale and summed these profiles together. This allows us to assess the performance of the instrument across different orders and examine the combined profiles.

In general, the fit results of Fe XIV line profiles at different orders are similar, especially when the S/N is high or after applying the 5-pixel average. In the brightest region of the AR, the differences in the Doppler shift and v_{eff} among various orders are typically less than $2\,\mathrm{km\,s^{-1}}$, which might be caused by the uncertainty of the absolute wavelength calibration. However, in the regions where the S/N is low, such as the AR at $1.5\,R_\odot$, and the fainter streamer, the difference in the Doppler velocity measurements in different orders may exceed 5–$10\,\mathrm{km\,s^{-1}}$.

The averaging along the slit and the summation of different orders greatly improve the S/N and result in more Gaussian-like profiles. The combination of various orders generally averages the Doppler shifts and line widths of individual profiles. We only used the strongest orders in the data analysis because the detectors were primarily focused on the strongest orders, which could potentially make the profiles asymmetric at weaker orders. However, the comparison highlights the potential of taking full advantage of multiple orders in future observations with caution, especially when the flatfield is properly made.

REFERENCES

Akinari, N. 2007, ApJ, 660, 1660, doi: 10.1086/512844

Antiochos, S. K., Mikić, Z., Titov, V. S., Lionello, R., & Linker, J. A. 2011, ApJ, 731, 112, doi: 10.1088/0004-637X/731/2/112

Aschwanden, M. J. 2005, Physics of the Solar Corona. An Introduction with Problems and Solutions (2nd edition) (Praxis Publishing Ltd)
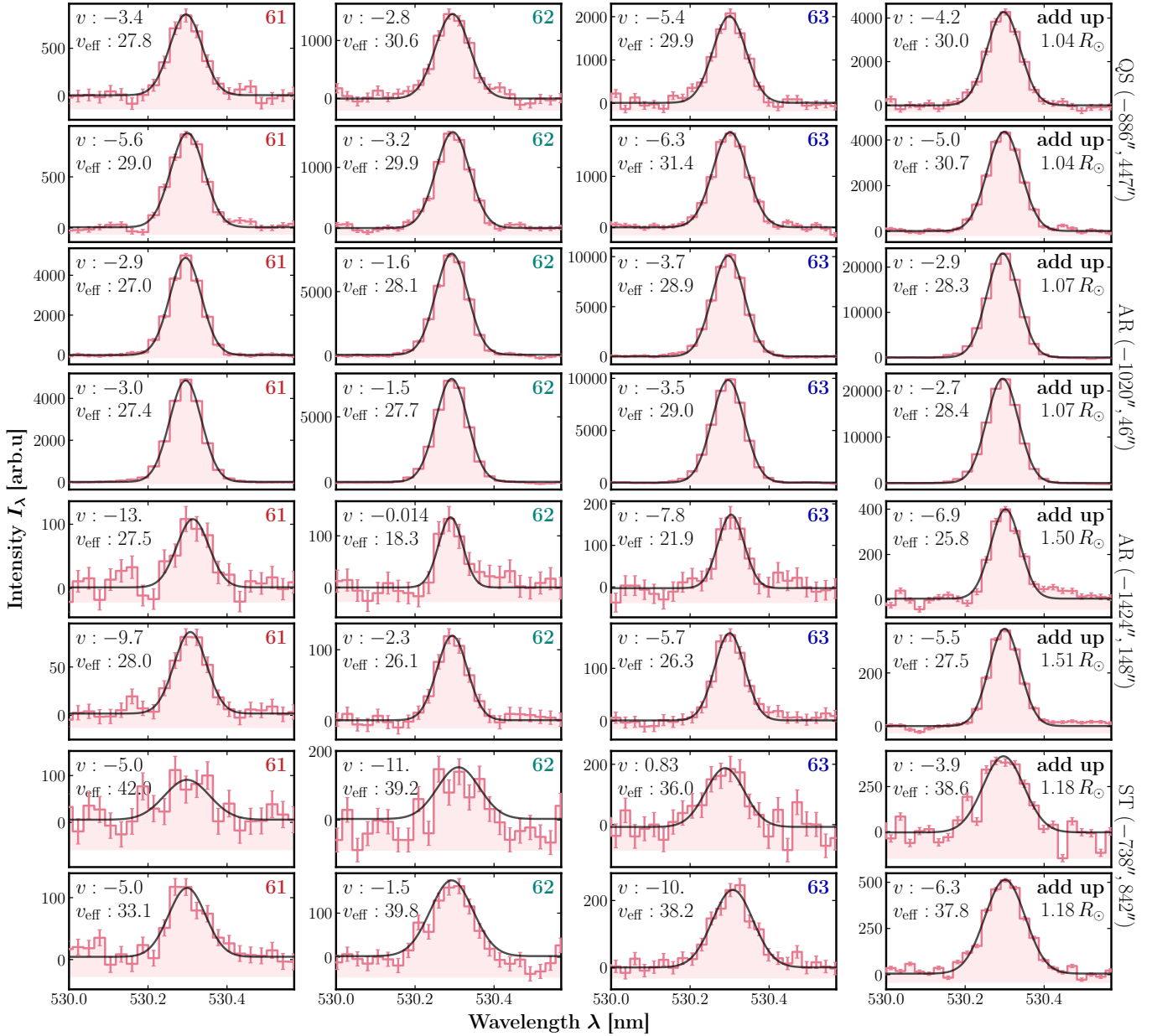
Figure 19. Comparison between Fe XIV 530.3 nm profiles at the 61st, 62nd, and 63rd orders in various coronal structures and heights: the QS, AR, and streamer (ST). The profiles in each structure are depicted in two rows of subplots: the first row shows the original profiles, while the second row displays the 5-pixel averaged profiles. The last row shows the sum of three different orders. The fit Doppler velocity v and effective velocity v_{eff} are measured in the units of $\mathrm{km\,s^{-1}}$. Link to the `Jupyter` notebook creating this figure: ⟳.

Aschwanden, M. J., Boerner, P., Schrijver, C. J., & Malanushenko, A. 2013, SoPh, 283, 5, doi: 10.1007/s11207-011-9876-5

Asgari-Targhi, M., van Ballegooijen, A. A., & Imada, S. 2014, ApJ, 786, 28, doi: 10.1088/0004-637X/786/1/28

Astropy Collaboration, Robitaille, T. P., Tollerud, E. J., et al. 2013, A&A, 558, A33, doi: 10.1051/0004-6361/201322068

Astropy Collaboration, Price-Whelan, A. M., Sipőcz, B. M., et al. 2018, AJ, 156, 123, doi: 10.3847/1538-3881/aabc4f

Astropy Collaboration, Price-Whelan, A. M., Lim, P. L., et al. 2022, apj, 935, 167, doi: 10.3847/1538-4357/ac7c74

Banerjee, D., Pérez-Suárez, D., & Doyle, J. G. 2009, A&A, 501, L15, doi: 10.1051/0004-6361/200912242

Banerjee, D., Teriaca, L., Doyle, J. G., & Wilhelm, K. 1998, A&A, 339, 208

Barnes, W., & Chen, B. 2022, wtbarnes/hissw: v2.3, v2.3, Zenodo, doi: 10.5281/zenodo.7352323

Bazin, C. 2013, PhD thesis, Aix-Marseille Université. http://www.theses.fr/2013AIXM4744

Boe, B., Downs, C., & Habbal, S. 2023, ApJ, 951, 55, doi: 10.3847/1538-4357/acd10b

Boe, B., Habbal, S., Downs, C., & Druckmüller, M. 2021, ApJ, 912, 44, doi: 10.3847/1538-4357/abea79

—. 2022, ApJ, 935, 173, doi: 10.3847/1538-4357/ac8101

Boe, B., Habbal, S., Druckmüller, M., et al. 2020, ApJ, 888, 100, doi: 10.3847/1538-4357/ab5e34

—. 2018, ApJ, 859, 155, doi: 10.3847/1538-4357/aabfb7

Bradski, G. 2000, Dr. Dobb's Journal of Software Tools

Brooks, D. H., & Warren, H. P. 2016, ApJ, 820, 63, doi: 10.3847/0004-637X/820/1/63

Brooks, D. H., Warren, H. P., Williams, D. R., & Watanabe, T. 2009, ApJ, 705, 1522, doi: 10.1088/0004-637X/705/2/1522

CoMP Team. 2011a, Coronal Multi-channel Polarimeter (CoMP) FeXIII 1074 nm Images, UCAR/NCAR - HAO/Mauna Loa Solar Observatory, doi: 10.5065/D6R78C8B

—. 2011b, Coronal Multi-channel Polarimeter (CoMP) FeXIII 1079 nm Images, UCAR/NCAR - HAO/Mauna Loa Solar Observatory, doi: 10.5065/D6MG7MJM

Contesse, L., Koutchmy, S., & Viladrich, C. 2004, Annales Geophysicae, 22, 3055, doi: 10.5194/angeo-22-3055-2004

Crameri, F. 2021, Scientific colour maps, 7.0.1, Zenodo, Zenodo, doi: 10.5281/zenodo.1243862

Cranmer, S. R. 1998, ApJ, 508, 925, doi: 10.1086/306415

Culhane, J. L., Harra, L. K., James, A. M., et al. 2007, SoPh, 243, 19, doi: 10.1007/s01007-007-0293-1

Del Zanna, G. 2013, A&A, 555, A47, doi: 10.1051/0004-6361/201220810

Del Zanna, G., & DeLuca, E. E. 2018, ApJ, 852, 52, doi: 10.3847/1538-4357/aa9edf

Del Zanna, G., Dere, K. P., Young, P. R., & Landi, E. 2021, ApJ, 909, 38, doi: 10.3847/1538-4357/abd8ce

Del Zanna, G., Gupta, G. R., & Mason, H. E. 2019, A&A, 631, A163, doi: 10.1051/0004-6361/201834625

Del Zanna, G., & Mason, H. E. 2018, Living Reviews in Solar Physics, 15, 5, doi: 10.1007/s41116-018-0015-3

Del Zanna, G., Weberg, M., & Warren, H. P. 2023, arXiv e-prints, arXiv:2308.06609, doi: 10.48550/arXiv.2308.06609

Dere, K. P., Landi, E., Mason, H. E., Monsignori Fossi, B. C., & Young, P. R. 1997, A&AS, 125, 149, doi: 10.1051/aas:1997368

Ding, A., & Habbal, S. R. 2017, ApJL, 842, L7, doi: 10.3847/2041-8213/aa7460

Dolla, L., & Solomon, J. 2008, A&A, 483, 271, doi: 10.1051/0004-6361:20077903

Doschek, G. A., & Feldman, U. 2000, ApJ, 529, 599, doi: 10.1086/308244

Duda, R. O., & Hart, P. E. 1972, Communications of the ACM, 15, 11, doi: 10.1145/361237.361242

Earl, N., Tollerud, E., O'Steen, R., et al. 2022, astropy/specutils: v1.9.1, v1.9.1, Zenodo, doi: 10.5281/zenodo.7348235

Edlén, B. 1943, ZA, 22, 30

Feldman, U., Doschek, G. A., Schühle, U., & Wilhelm, K. 1999, ApJ, 518, 500, doi: 10.1086/307252

Freeland, S. L., & Handy, B. N. 2012, SolarSoft: Programming and data analysis environment for solar physics. http://ascl.net/1208.013

Gilly, C. R., & Cranmer, S. R. 2020, ApJ, 901, 150, doi: 10.3847/1538-4357/abb1ad

Grotrian, W. 1939, Naturwissenschaften, 27, 214, doi: 10.1007/BF01488890

Gupta, G. R. 2017, ApJ, 836, 4, doi: 10.3847/1538-4357/836/1/4

Gupta, G. R., Del Zanna, G., & Mason, H. E. 2019, A&A, 627, A62, doi: 10.1051/0004-6361/201935357

Habbal, S. R., Morgan, H., Johnson, J., et al. 2007, ApJ, 663, 598, doi: 10.1086/518403

Habbal, S. R., Druckmüller, M., Morgan, H., et al. 2011, ApJ, 734, 120, doi: 10.1088/0004-637X/734/2/120

Habbal, S. R., Druckmüller, M., Alzate, N., et al. 2021, ApJL, 911, L4, doi: 10.3847/2041-8213/abe775

Hahn, M., Asgari-Targhi, M., & Savin, D. W. 2023, ApJ, 953, 3, doi: 10.3847/1538-4357/acdfd2

Hahn, M., Bryans, P., Landi, E., Miralles, M. P., & Savin, D. W. 2010, ApJ, 725, 774, doi: 10.1088/0004-637X/725/1/774

Hahn, M., Landi, E., & Savin, D. W. 2012, ApJ, 753, 36, doi: 10.1088/0004-637X/753/1/36

Hara, H., & Ichimoto, K. 1999, ApJ, 513, 969, doi: 10.1086/306880

Hassler, D. M., & Moran, T. G. 1994, SSRv, 70, 373, doi: 10.1007/BF00777895

Hassler, D. M., Rottman, G. J., Shoub, E. C., & Holzer, T. E. 1990, ApJL, 348, L77, doi: 10.1086/185635

Hunter, J. D. 2007, Computing in Science & Engineering, 9, 90, doi: 10.1109/MCSE.2007.55

Imada, S., Hara, H., & Watanabe, T. 2009, ApJL, 705, L208, doi: 10.1088/0004-637X/705/2/L208

Jefferies, J. T., Orrall, F. Q., & Zirker, J. B. 1971, SoPh, 16, 103, doi: 10.1007/BF00154505

Kamio, S., Fredvik, T., & Young, P. 2019, EIS Software Note No. 5 - Orbital drift of the EIS wavelength scale. https://sohoftp.nascom.nasa.gov/solarsoft/hinode/eis/doc/eis_notes/05_WAVELENGTH_CORRECTION/eis_swnote_05.pdf

Kamio, S., & Mariska, J. T. 2012, SoPh, 279, 419, doi: 10.1007/s11207-012-0014-9

Kim, I. S. 2000, in Astronomical Society of the Pacific Conference Series, Vol. 205, Last Total Solar Eclipse of the Millennium, ed. W. Livingston & A. Özgüç, 69

Kosugi, T., Matsuzaki, K., Sakao, T., et al. 2007, SoPh, 243, 3, doi: 10.1007/s11207-007-9014-6

Koutchmy, S., Baudin, F., Abdi, S., Golub, L., & Sèvre, F. 2019, A&A, 632, A86, doi: 10.1051/0004-6361/201935681

Koutchmy, S., Contesse, L., Viladrich, C., Vilinga, J., & Bocchialini, K. 2005, in ESA Special Publication, Vol. 11, The Dynamic Sun: Challenges for Theory and Observations, ed. D. Danesy, S. Poedts, A. de Groof, & J. Andries, 26.1

Laming, J. M., Feldman, U., Schühle, U., et al. 1997, ApJ, 485, 911, doi: 10.1086/304465

Landi, E. 2007, ApJ, 663, 1363, doi: 10.1086/517910

Landi, E., & Cranmer, S. R. 2009, ApJ, 691, 794, doi: 10.1088/0004-637X/691/1/794

Landi, E., & Feldman, U. 2003, ApJ, 592, 607, doi: 10.1086/375562

Lemen, J. R., Title, A. M., Akin, D. J., et al. 2012, SoPh, 275, 17, doi: 10.1007/s11207-011-9776-8

Massey, P., Valdes, F., & Barnes, J. 1992, IRAF User Guide, 2

Mierla, M., Schwenn, R., Teriaca, L., Stenborg, G., & Podlipnik, B. 2008, A&A, 480, 509, doi: 10.1051/0004-6361:20078329

Mihalas, D. 1978, Stellar atmospheres (W. H. Freeman and Company)

Mikić, Z., Downs, C., Linker, J. A., et al. 2018, Nature Astronomy, 2, 913, doi: 10.1038/s41550-018-0562-5

Moran, T. G. 2003, ApJ, 598, 657, doi: 10.1086/378795

Morton, R. J., Tomczyk, S., & Pinto, R. 2015, Nature Communications, 6, 7813, doi: 10.1038/ncomms8813

Müller, D., St. Cyr, O. C., Zouganelis, I., et al. 2020, A&A, 642, A1, doi: 10.1051/0004-6361/202038467

Muro, G. D., Gunn, M., Fearn, S., Fearn, T., & Morgan, H. 2023, SoPh, 298, 75, doi: 10.1007/s11207-023-02162-1

Oliphant, T. E. 2006, A guide to NumPy, Vol. 1 (Trelgol Publishing USA)

Pesnell, W. D., Thompson, B. J., & Chamberlin, P. C. 2012, SoPh, 275, 3, doi: 10.1007/s11207-011-9841-3

Prabhakar, M., & Raju, K. P. 2022, ApJ, 931, 40, doi: 10.3847/1538-4357/ac610e

Prabhakar, M., Raju, K. P., & Chandrasekhar, T. 2019, SoPh, 294, 26, doi: 10.1007/s11207-019-1409-7

Raju, K. P., Chandrasekhar, T., & Ashok, N. M. 2011, ApJ, 736, 164, doi: 10.1088/0004-637X/736/2/164

Raju, K. P., Desai, J. N., Chandrasekhar, T., & Ashok, N. M. 1991, Journal of Astrophysics and Astronomy, 12, 311, doi: 10.1007/BF02702319

Seely, J. F., Feldman, U., Schühle, U., et al. 1997, ApJL, 484, L87, doi: 10.1086/310769

Shi, T., Manchester, Ward, I., Landi, E., et al. 2022, ApJ, 928, 34, doi: 10.3847/1538-4357/ac52ab

Singh, J., Hasan, S. S., Gupta, G. R., Nagaraju, K., & Banerjee, D. 2011, SoPh, 270, 213, doi: 10.1007/s11207-011-9732-7

Singh, J., Sakurai, T., & Ichimoto, K. 2006, ApJ, 639, 475, doi: 10.1086/499200

Singh, J., Sakurai, T., Ichimoto, K., Suematsu, Y., & Takeda, A. 2002, PASJ, 54, 793, doi: 10.1093/pasj/54.5.793

The SunPy Community, Barnes, W. T., Bobra, M. G., et al. 2020, The Astrophysical Journal, 890, 68, doi: 10.3847/1538-4357/ab4f7a

Tian, H., Tomczyk, S., McIntosh, S. W., et al. 2013, SoPh, 288, 637, doi: 10.1007/s11207-013-0317-5

Tomczyk, S., Card, G. L., Darnell, T., et al. 2008, SoPh, 247, 411, doi: 10.1007/s11207-007-9103-6

Tu, C. Y., Marsch, E., Wilhelm, K., & Curdt, W. 1998, ApJ, 503, 475, doi: 10.1086/305982

Ugarte-Urra, I. 2010, EIS Software Note No. 12 - Stray light. http://solarb.mssl.ucl.ac.uk/SolarB/eis_docs/eis_notes/12_STRAY_LIGHT/eis_swnote_12.pdf

van der Holst, B., Sokolov, I. V., Meng, X., et al. 2014, ApJ, 782, 81, doi: 10.1088/0004-637X/782/2/81

Van Der Walt, S., Colbert, S. C., & Varoquaux, G. 2011, Computing in Science & Engineering, 13, 22

Virtanen, P., Gommers, R., Oliphant, T. E., et al. 2020, Nature Methods, 17, 261, doi: https://doi.org/10.1038/s41592-019-0686-2

Warren, H. P., Ugarte-Urra, I., & Landi, E. 2014, ApJS, 213, 11, doi: 10.1088/0067-0049/213/1/11

Wilhelm, K., Fludra, A., Teriaca, L., et al. 2005, A&A, 435, 733, doi: 10.1051/0004-6361:20042460

Wilhelm, K., Marsch, E., Dwivedi, B. N., et al. 1998, ApJ, 500, 1023, doi: 10.1086/305756

Withbroe, G. L., & Noyes, R. W. 1977, ARA&A, 15, 363, doi: 10.1146/annurev.aa.15.090177.002051

Zhu, Y., Habbal, Shadia R. Ding, A., Yamashiro, B., et al. 2024, Spectroscopic Observations of the Solar Corona during the 2017 August 21 Total Solar Eclipse: Comparison of Spectral Line Widths and Doppler Shifts Between Open and Closed Magnetic Structures, 0.0.2, Zenodo, doi: 10.5281/zenodo.10801930

Zhu, Y., Szente, J., & Landi, E. 2021, ApJ, 913, 74, doi: 10.3847/1538-4357/abf1e3

—. 2023, ApJ, 948, 90, doi: 10.3847/1538-4357/acc187